



HAL
open science

Mechanism of material deformation during cavitation bubble collapse

Prasanta Sarkar, Giovanni Ghigliotti, Jean-Pierre Franc, Fivel Marc

► **To cite this version:**

Prasanta Sarkar, Giovanni Ghigliotti, Jean-Pierre Franc, Fivel Marc. Mechanism of material deformation during cavitation bubble collapse. *Journal of Fluids and Structures*, 2021, 105, pp.103327. 10.1016/j.jfluidstructs.2021.103327 . hal-03326078

HAL Id: hal-03326078

<https://hal.science/hal-03326078>

Submitted on 25 Aug 2021

HAL is a multi-disciplinary open access archive for the deposit and dissemination of scientific research documents, whether they are published or not. The documents may come from teaching and research institutions in France or abroad, or from public or private research centers.

L'archive ouverte pluridisciplinaire **HAL**, est destinée au dépôt et à la diffusion de documents scientifiques de niveau recherche, publiés ou non, émanant des établissements d'enseignement et de recherche français ou étrangers, des laboratoires publics ou privés.

Mechanism of material deformation during cavitation bubble collapse

Prasanta Sarkar ^{a,*}, Giovanni Ghigliotti^a, Jean-Pierre Franc^a, Marc Fivel^b

^aUniv. Grenoble Alpes, CNRS, Grenoble INP, LEGI, 38000 Grenoble, France

^bUniv. Grenoble Alpes, CNRS, Grenoble INP, SIMaP, 38000 Grenoble, France

Abstract

This research is devoted to understanding the physical mechanism of cavitation erosion in liquid flows at the fundamental scale of cavitation bubble collapse. Cavitation bubbles form in a liquid when the pressure of the liquid decreases locally below the saturated vapor pressure p_v^{sat} . The bubbles grow due to low ambient pressure and collapse when the surrounding liquid pressure increases again above p_v^{sat} . Bubble collapse near solid walls can result in high velocity liquid jet and shock wave emission that cause high pressure loads on the wall. These pressure loads are responsible for the erosive damages on solid surfaces, as observed in applications like liquid fuel injection, hydrodynamic power generation and marine propulsion (Brujan (2011), Franc et al. (2012)). On the other hand, the pressure loads from collapsing bubbles are exploited for applications like shock wave lithotripsy, drug delivery and cleaning surfaces (Lauterborn and Vogel (2013)). In this work, we follow a numerical approach, which begins with the development of a compressible solver capable of resolving the cavitation bubbles in the finite-volume code YALES2¹ employing a simplified homogeneous mixture model. The solid material response to cavitation loads is resolved with the finite element code Cast3M². A one-way coupling approach for fluid-structure interaction (FSI) simulation between the fluid and solid domains is pursued. In this simple approach, the pressure field computed by the fluid solver at the fluid-solid interface is communicated to the solid solver which computes the deformation induced in the material. In the end, the dynamical events responsible for surface deformation are highlighted from 2D vapor bubble collapse dynamics and associated pressure loads on the solid wall are estimated. The response of different materials to bubbles collapsing at different distances from the solid wall is discussed.

Keywords: cavitation; cavitation erosion; fluid-structure interaction; one-way coupling; computational fluid dynamics; compressible flows

*. Corresponding author.

1. <http://yales2.coria-cfd.fr>

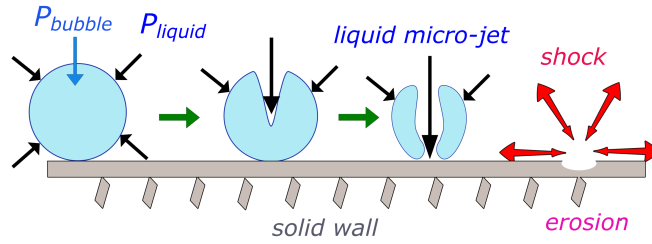
2. <http://www-cast3m.cea.fr>

1. Introduction

The motivation of this research is understanding the physical mechanism of cavitation erosion in compressible liquid flows, with applications in the field of aerospace, hydrodynamics, automotive, bioengineering etc. Cavitation is the appearance of vapor regions (or cavities) inside an initially homogeneous liquid when the pressure decreases locally (Brennen (1995), Franc and Michel (2006)). Analogous to boiling where water turns into vapor when the temperature reaches the boiling point, in cavitation the phase change from water into vapor takes place when the pressure decreases below its vapor pressure. The formation of the bubbles or nucleation in liquid water is however quite complex, as pure water is able to sustain pressure below the vapor pressure before the intermolecular bonds break for the formation of cavities. In practice, microscopic dissolved gas or solid impurities, known as cavitation nuclei, act as weak points in the continuum liquid where the cavities grow once the vapor pressure is reached. Bubbles grow by vaporisation of liquid water as long as the local pressure is below saturation pressure. When the local pressure increases again above vapor pressure, the condensation of water vapor causes the bubble to reabsorb. Due to liquid inertia the reabsorption is usually relatively slow at the initial phase, but becomes extremely rapid at the final stages, this phenomenon is referred to as collapse. Pressure variations in a flow are given by the flow dynamics in a given geometry, so the flow geometry together with flow inlet and outlet conditions determines the regions of bubble formation and bubble collapse. The collapse of vapor structures can generate the emission of intense shock waves and also fast and focused liquid jets. Both are known to generate local pressures that can be extremely high, often in the GPa range.

Cavitation affects the performance and life cycle of a machine by producing unwanted noise and vibrations, but also surface erosion, depending on the location, duration and extent of the exposure to cavitating flows (Akcabay and Young (2014), Hsiao and Chahine (2015)). Bubble collapse, if close to a solid boundary, is believed to be causing the surface damage. The first numerical solution for bubble collapse and rebound (or re-growth of bubble volume after collapse) considering the compressibility of liquid water was proposed by Hickling and Plesset (1964), which showed the emission of shock wave at the instant of rebound, propagating outwards from the bubble center. The dynamics of collapsing bubble in an compressible liquid medium was further studied by Fujikawa and Akamatsu (1980), Prosperetti (1987). On the dynamics of non-spherical bubble collapse, Naude and Ellis (1961) and Benjamin and Ellis (1966) showed successfully that cavitation bubbles do not collapse spherically near solid boundaries and explained the acceleration of a translating bubble cavity during its collapse, coupled with the formation of a liquid micro-jet and formation of bubble vortex ring.

The presence of a boundary retards the acceleration of surrounding liquid and as a result, the liquid surrounding the bubble surface located far from the solid wall attains a higher velocity. This high velocity of surrounding liquid near the bubble surface far from the wall in comparison to the bubble surface closer to solid wall gives rise to a liquid jet. The re-entrant liquid jet pierces through the bubble surface opposite to the solid wall, thus accelerating one side of the bubble towards the opposite surface. The velocity of the liquid jet was predicted to be very high, on the order of few hundred m/s , which led to the hypothesis that the liquid jet piercing the bubble and hitting the solid wall in a non-spherical collapse is the primary cause of cavitation erosion. Many decades later, this hypothesis is still debatable, nevertheless a much advanced review of the features of liquid micro-jet properties can be found in Blake and Gibson (1987) and Obreschkow et al. (2011). The collapse of a vapor bubble surrounded by a liquid can be represented as in fig. 1, where p_{bubble} is the pressure inside the bubble and p_{liquid} is the surrounding liquid pressure such that $p_{liquid} \gg p_{bubble}$.



Bubble collapse near a solid boundary

FIGURE 1: Vapor bubble collapse due to imposed pressure difference $p_{liquid} \gg p_{bubble}$: non-spherical bubble collapse near a solid wall.

The liquid jet is directed towards the solid wall and multiple shock waves are emitted due to the impact of the liquid jet with the opposite bubble surface and eventually, the solid wall. This highly dynamical sequence of events along with high amplitude pressure peaks at the solid wall from emitted shock waves and liquid jet needs to be resolved first to predict material response. Further insights on numerical simulations of bubble collapse are provided by Johnsen and Colonius (2009), Müller et al. (2010), Lauer et al. (2012) and on bubble collapse near deformable surfaces by Gibson and Blake (1980), Gibson and Blake (1982).

Cavitation erosion takes place on concentrated areas of solid walls exposed to cavitation. Collapses of vapor structures exert forces on the solid surface, leading to high stress levels on and in the solid. A detailed review of hydrodynamic cavitation erosion has been reported in Franc (2009), Brujan (2011), Franc et al. (2012). Considerable research has focused on understanding the physics of bubble formation and collapse near solid boundaries. However to date, a thorough understanding of how bubble collapse relates to surface erosion has been an elusive

goal due to the different physical processes of fluids and solids, different temporal scales of bubble collapse ($\sim ms$) and cavitation erosion (\sim months, years) and computational limitations. As explained in [Franc and Michel \(2006\)](#), an elastic wall would see a much smaller impact pressure compared to the rigid wall from a high velocity liquid jet due to the damping effect of the wall whose displacement allows for pressure to relax in the fluid. Therefore, the logical extension is the fluid-structure interaction (FSI) study resolving both the fluid and solid dynamics during cavitation bubble collapse ([Kalumuck et al. \(1995\)](#), [Hsiao et al. \(2014\)](#), [Choi and Chahine \(2016\)](#), [Joshi et al. \(2019\)](#)).

This research work thus focuses on developing a computational model of bubble collapse dynamics close to a solid wall with FSI to aid in the development of cavitation erosion prediction tools. A FSI methodology has been pursued by combining Computational Fluid Dynamics (*CFD*) and Computational Solid Mechanics (*CSM*) on the scale of single bubble collapse. The focus is to develop the required methodology in the CFD solver YALES2 and CSM solver CAST3M to model accurately a 2D bubble collapse near a rigid wall and predict material surface deformation with one-way FSI. One-way coupling is intended from the fluid to the solid only, in order to study the response of the solid to the fluid load. In one-way FSI, the feedback of solid wall deformation is not considered on the fluid dynamics. In the scope of this paper, there will be no effect of material surface deformation on the evolving dynamics of the collapsing cavitation bubble. Despite this simplification, one-way coupling is desirable both from a methodological point of view (as a first step towards two-way FSI coupling in which the feedback of solid wall deformation on the fluid is considered) and from an operational point of view (the numerical simulation tools need not to be integrated one with the other).

This paper is structured as follows : Section 2 introduces the CFD and CSM solver methodology along with one-way FSI approach ; Section 3 presents the 2D bubble collapse dynamics ; Section 4 discusses the material response to the pressure loads from collapsing bubbles followed by conclusions drawn in Section 5.

2. Numerical approach

2.1. Compressible flow solver

The numerical approach for simulating compressible cavitating flow is developed with the multi-physics solver YALES2 based on the *finite volume method*. The solver is based on the pressure-based semi-implicit algorithm developed by [Moureau et al. \(2007\)](#) for ideal gas flows. The *Navier-Stokes* equations in eq. (1) & (2) for the conservation of mass and momentum forms the system of conservation equations in our fluid flow modelling.

$$\frac{\partial \rho}{\partial t} + \nabla \cdot (\rho \underline{u}) = 0 \quad (1)$$

$$\frac{\partial \rho \underline{u}}{\partial t} + \nabla \cdot (\rho \underline{u} \otimes \underline{u}) = -\nabla p + \nabla \cdot \underline{\tau} \quad (2)$$

Here, ρ is the fluid density, \underline{u} is the velocity, p is the pressure, $\underline{\tau}$ is the viscous stress tensor, t is the time, (∇) is the gradient operator, $(\nabla \cdot)$ is the divergence operator. In our cavitation modelling approach, the fluid is assumed to be barotropic (i.e. pressure depends on density only) and hence the energy equation is not used. In incompressible flows, no pressure and density fluctuations are created due to the velocity field. Consequently, the time step size of a numerical simulation is limited by the Courant-Friedrichs-Lewy (*CFL*) condition in eq. (3) which determines the distance travelled by the fluid moving with the convective velocity \underline{u} .

$$CFL = |\underline{u}| \frac{\Delta t}{\Delta x} < 1 \quad (3)$$

Here, Δt is the given time step and Δx is the mesh size. To resolve acoustic wave propagation in compressible flows, the finite propagation speed of the waves is defined by the speed of sound c . This isentropic speed of sound is therefore :

$$c = \sqrt{\frac{\partial p}{\partial \rho}} \quad (4)$$

The compressible set of governing equations are hyperbolic in nature and any fluctuation is transported at the speed of sound, so $\underline{u} \pm c$ in 1D. The dimensionless quantity describing the ratio of convective velocity \underline{u} to the speed of sound c , is the Mach number $Ma = \underline{u}/c$. The relationship between Courant-Friedrichs-Lewy condition with acoustic propagation CFL_{acou} for compressible flow and convective CFL for incompressible flow is expressed as :

$$\begin{aligned} CFL_{acou} &= |\underline{u} + c| \frac{\Delta t}{\Delta x} = \frac{\underline{u} \Delta t}{\Delta x} \left(1 + \frac{1}{Ma} \right) \\ CFL_{acou} &= CFL \left(1 + \frac{1}{Ma} \right) \\ CFL_{acou} &\left(\frac{Ma}{Ma + 1} \right) = CFL \end{aligned} \quad (5)$$

For a compressible flow simulation, the time step derived from the minimum of (CFL, CFL_{acou}) will be usually limited by the CFL_{acou} condition. For a cavitation bubble collapse in liquid water with $c = 1483 \text{ m/s}$, the Mach number stays small for major part of the simulation and approaches $Ma = 1$ only during the final stages of bubble collapse. An explicit treatment of the time step will lead to very small time steps for such simulation and larger computation time. Thus, the solver's design down to the algorithmic level has an effect on the capability to resolve such problems efficiently.

The weak form or so-called integral form of the compressible *Navier-Stokes* equations are solved in our solver, which allows to model discontinuities like shock waves and phase boundaries in a cavitating flow. In the *prediction-correction* numerical algorithm used, flow convection and acoustics are separated and time advancement is performed based on the characteristic splitting of the compressible *Navier-Stokes* equations. The prediction-correction algorithm solves for the purely convective part of governing equations explicitly in the first step with a constant acoustic source term for $\phi \in (\rho, \underline{m})$ as in eq. (6) & (7), where $\underline{m} = \rho \underline{u}$ is the momentum.

$$\frac{\rho^* - \rho^n}{\Delta t} + \nabla \cdot (\tilde{\rho} \underline{u}^n) - (\tilde{\rho} - \rho^n) \nabla \cdot \underline{u}^n = 0 \quad (6)$$

$$\frac{\underline{m}^* - \underline{m}^n}{\Delta t} + \nabla \cdot (\tilde{\underline{m}} \otimes \underline{u}^n) - (\tilde{\underline{m}} - \underline{m}^n) \nabla \cdot \underline{u}^n = -\nabla p^n + \nabla \cdot \underline{\underline{\tau}}^n \quad (7)$$

The speed of sound c^n at time step n is computed before starting the time advancement to obtain the time step from CFL_{acou} . A characteristic analysis of the system of equations of this step shows that the eigenvalues are equal to the convective propagation speed \underline{u} and the step is only limited by the convective CFL stability condition, independently of Mach number. For $\phi \in (\rho, \underline{m})$ in eq. (6) & (7), ϕ^n is the value of ϕ before time advancement i.e. from the previous time step, ϕ^* is the value computed at the end of the prediction step and $\tilde{\phi}$ is the value computed at different steps of the time integration scheme. The stress terms for pressure and momentum diffusion are explicit contributions, evaluated only at the beginning of the time step. At the end of the prediction step, the equation of state is used to estimate the intermediate pressure p^* from ρ^* .

It is worth noting here that this implementation is being specifically developed for modeling cavitating flows in liquid water, which will be modeled with a barotropic equation of state. A barotropic assumption implies that the pressure is only a function of density $p = f(\rho)$. Therefore, the evolution of energy equation is decoupled from the solver algorithm and by virtue of it, temperature evolution is not resolved in our system of governing equations for the compressible cavitation solver.

In the prediction step only eq. (6) & (7) are spatially discretized with a fourth-order centered scheme (Malandain (2013), Roger et al. (2016)). The time integration scheme TFV4A developed by Kraushaar (2011) has been used to advance the solution in time from t_n to an instant $t_{n+1} = t_n + \Delta t$, where Δt is the time step used. This fourth-order scheme is explicit in nature, and only uses the known solution at t_n . The scheme is based on the idea of blending the low storage, explicit, fourth-order Runge-Kutta with a Lax-Wendroff-type scheme, where the in-built numerical diffusion in the temporal scheme can be adjusted.

The speed of sound c^* is updated at the end of the prediction step based on the advected density field. This is especially important for multiphase flows where

the different phases/components of the fluid can have varying orders of speed of sound. The computation of speed of sound from the advected density at each control volume is important near phase boundaries i.e. interfaces. Thus in the correction step, the subsequent pressure field computation will have the correct speed of sound of the fluid phase from the temporal evolution of density, most importantly near fluid interfaces.

Before correcting the conservative variable in second step, the Helmholtz equation is solved implicitly with the Stabilized Bi-Conjugate Gradient (BiCGSTAB2) linear solver (Vantighem (2011)) for the pressure correction $\delta p = p^{n+1} - p^*$ in eq. (8). The equation is derived by taking the divergence of momentum equation during the correction step and using the continuity equation from the prediction step to remove the unknown momentum \underline{m}^{n+1} . Thus, a discrete mass-conserving equation for the corrected pressure p^{n+1} and pressure variation δp is obtained. The second term on the LHS represents the influence of local flow on the acoustics. The second and third term in LHS are negligible for low Mach number flows and the Helmholtz equation with negligible acoustic presence tends towards a variable density Poisson equation.

$$\begin{aligned} \nabla \cdot \nabla (p^{n+1} - p^*) - \nabla \cdot \frac{\underline{u}^n}{(c^*)^2 \Delta t} (p^{n+1} - p^*) - \frac{p^{n+1} - p^*}{(c^*)^2 \Delta t^2} \\ = \nabla \cdot \nabla (p^n - p^*) + \frac{\rho^* - \rho^n}{\Delta t^2} + \frac{1}{\Delta t} \nabla \cdot (\rho^* \underline{u}^*) \end{aligned} \quad (8)$$

The governing equations for the correction step are obtained after removing eq. (6) & (7) used in the prediction step from the full set of *Navier-Stokes* equations in eq. (1) & (2). A temporal integration of the resulting equation after splitting resolves the acoustic influence on the set of conservative variable $\phi \in (\rho, \underline{m})$, taking into account the presence of acoustic source term in the prediction step. In the correction step the pressure variation is used to express the variations of the conserved variables in eq. (9) & (10) obtaining the updated field of ρ^{n+1} & \underline{m}^{n+1} .

$$\frac{\rho^{n+1} - \rho^*}{\Delta t} - \frac{1}{(c^*)^2} \frac{\delta p}{\Delta t} = 0 \quad (9)$$

$$\frac{\underline{m}^{n+1} - \underline{m}^*}{\Delta t} - \frac{\underline{u}^n}{(c^*)^2} \frac{\delta p}{\Delta t} = -\nabla (\delta p) \quad (10)$$

The pressure $p^{(n+1)c}$ is computed again from the updated density ρ^{n+1} through the equation of state at the end of the correction step. This is to enforce strict agreement between pressure and density in the phase interfaces for cavitating flows, in agreement with the barotropic assumption. The discontinuities in the orders of magnitude of density and speed of sound at the interface between vapor and liquid regions can often give rise to numerical oscillations in the pressure

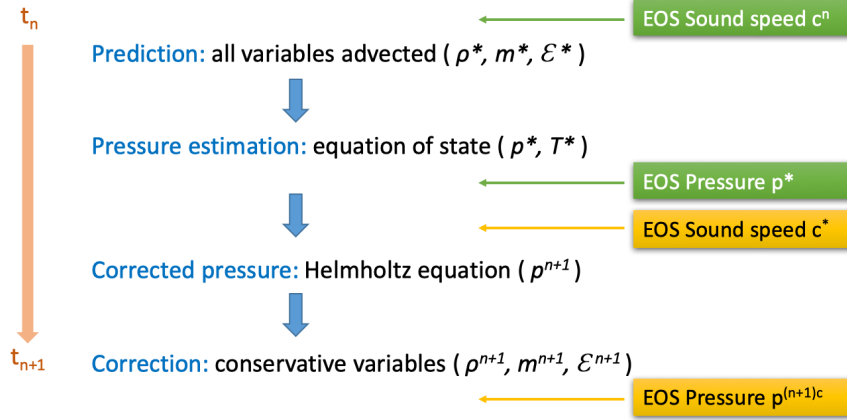


FIGURE 2: Schematic of solver algorithm- (in yellow) modified algorithm to estimate intermediate sound speed and corrected pressure from equation of state.

field. A situation may arise where the corrected p^{n+1} and ρ^{n+1} do not satisfy the equation of state in specific regions of phase interface.

A *single fluid* or widely called homogeneous mixture model is used to treat the two-phase cavitating flow. A single fluid model treats the cavitating flow as a mixture of two fluids of varying density and are quite popular in cavitation studies (Goncalves and Patella (2009)). A homogeneous mixture of liquid and vapor is assumed in two phase regions, with vapor volume fraction $\alpha = \Omega_v/\Omega$, where Ω_v is the vapor volume in a control volume Ω . The volume average density ρ in the two phase region is expressed by the linear combination of liquid density ρ_l and vapor density ρ_v in as :

$$\rho = \alpha\rho_v + (1 - \alpha)\rho_l \quad (11)$$

The model assumes local kinematic equilibrium between phases which implies same local velocity for both phases and thermodynamic equilibrium. The later hypothesis implies that the phase change is infinitely fast, isentropic and in mechanical equilibrium. This allows us to distinguish the different phases in the model - pure liquid water with $\alpha = 0$ and a two phase liquid-vapor mixture region separated from the pure liquid by $\rho_{sat,l}$ in eq. (12).

$$\alpha = \begin{cases} 0 & , \rho \geq \rho_{sat,l} \\ \frac{\rho_{sat,l} - \rho}{\rho_{sat,l} - \rho_{sat,v}} & , \rho < \rho_{sat,l} \end{cases} \quad (12)$$

Here, $\rho_{sat,l}$ and $\rho_{sat,v}$ are the liquid and vapor densities at the saturation point, respectively. In literature, homogenous mixture models have been used to resolve large vapor structures like cavitating vortices or bubble clouds as well as single bubbles. It does not require any empirically computed mass transfer term between

the liquid and vapor phases. However since no interface is reconstructed in the model, the surface tension effects are neglected.

The different phases are defined by equations of state which are barotropic, meaning that the pressure is a function of the fluid density only. These equations are used in the solver to evaluate analytically the pressure p from the density ρ . The two-phase liquid-vapor mixture region is considered without the presence of any non-condensable gas. The pure liquid phase is modelled with the modified Tait equation of state in eq. (13), with the fitted model constants B and N given in table 1.

$$p = (p_{sat} + B) \left(\frac{\rho}{\rho_{sat,l}} \right)^N - B, \text{ if } \alpha = 0 \quad (13)$$

In the two phase mixture region, phase transition is modelled following an isen-

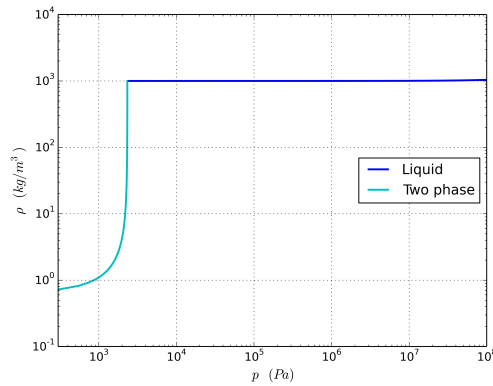


FIGURE 3: Density vs pressure evolution in the cavitation model.

tropic path in the phase diagram proposed by Egerer et al. (2013) in eq. (14), where the model constant C and saturation properties are taken at a reference temperature $T_{ref} = 293.15 K$, listed in table 1. The equilibrium pressure-density evolution following an isentropic path in the phase diagram is shown in fig. 3.

$$p = p_{sat} + C \left(\frac{1}{\rho_{sat,l}} - \frac{1}{\rho} \right), \text{ if } 0 < \alpha < 1 \quad (14)$$

A consistent speed of sound based on isentropic relationship in eq. (4) is used for the pure liquid as follows :

$$c = \sqrt{(p_{sat} + B) N \frac{(\rho)^{N-1}}{(\rho_{sat,l})^N}}, \text{ if } \alpha = 0 \quad (15)$$

The speed of sound in the homogeneous two-phase liquid-vapor mixture based on the two-phase equation of state decreases dramatically as the fluid is not composed of a single liquid phase anymore. This huge decrease in speed of sound

at the phase interface, plotted in fig. 4 as “Isentropic two phase”, makes the flow locally supersonic as soon as cavitation appears, and could give rise to spurious numerical oscillations at the interface. As the purview of this work is the collapse of cavitation bubbles and resulting pressure wave propagation in the liquid medium, a constant speed of sound is implemented in the two-phase cavitation region shown in fig. 4 as “Two phase”. In our numerical simulations, the shock

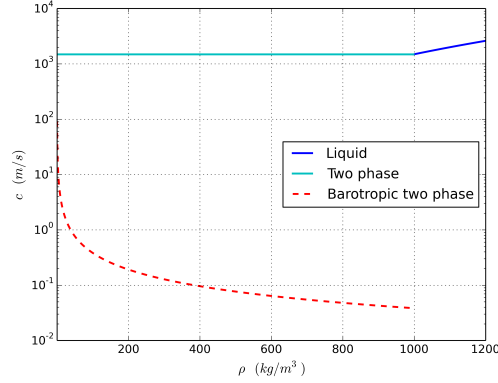


FIGURE 4: Speed of sound vs density evolution in the cavitation model.

waves propagating in the pure liquid are resolved accurately and shock propagation speed in the two-phase cavitation region is assumed not to be relevant. The shock propagation in the two phase region inside the bubble propagates at a constant speed of sound of 1483.3 m/s , obtained from the $\rho_{sat,l}$ at 293.15 K . The model constants used in the cavitation model are summarized in table 1.

Property	Value	Unit
p_{sat}	2340	Pa
$\rho_{sat,l}$	998.1618	kg/m^3
$\rho_{sat,v}$	0.01731	kg/m^3
$\mu_{sat,l}$	1.002×10^{-3}	$Pa \cdot s$
$\mu_{sat,v}$	9.727×10^{-6}	$Pa \cdot s$
C	1468.54	$Pa \cdot kg/m^3$
N	7.132	—
B	3.078×10^8	Pa
T_{ref}	293.15	K

TABLE 1: Saturation properties of water.

For viscous calculations, a constant liquid viscosity $\mu_{sat,l}$ is used for pure liquid phase whereas the implemented dynamic viscosity for the liquid-vapor mixture is

given in eq. (16) :

$$\mu = (1 - \alpha) \left(1 + \frac{5}{2} \alpha \right) \mu_{sat,l} + \alpha \mu_{sat,v}, \text{ if } 0 < \alpha < 1 \quad (16)$$

The effective viscosity for liquid-vapor mixture is modelled as a quadratic law with a maximum in the two phase region following the model proposed in [Beattie and Whalley \(1982\)](#). The dynamic viscosity varies with the vapor volume fraction α in the two phase region. In general, the high order centred space discretization schemes used are oscillatory in nature. In the regions of numerical discontinuities like wave fronts, the application of such schemes results in non-physical, spurious oscillations. Their combination with Runge-Kutta type methods can become unstable and stabilizing measures need to be taken with strategies like numerical diffusion in spatial and temporal discretization, adding artificial viscosity, high-order filtering of solution fields. A nonlinear artificial viscosity proposed by [Cook and Cabot \(2004\)](#), based on the high-order derivative of the strain rate tensor is used to damp spurious oscillations near discontinuities. A mesh dependent artificial viscosity μ_{artif} is added to the momentum equation, defined as :

$$\mu_{artif} = C_{\mu} \rho (\Delta x)^r \overline{\left| \frac{\partial^r u}{\partial x^r} \right|} \quad (17)$$

where Δx is the mesh spacing, $\overline{\left| \cdot \right|}$ is a Gaussian filter applied to the absolute value to ensure a smooth and positive μ_{artif} . C_{μ} is a model constant called the artificial viscosity constant and r is a user-specified integer called the artificial viscosity order and is set to 4 wherever applicable. Additionally, a high order filtering of the solution variables based on volume-weighted averaging with a Gaussian-type smoothing has been employed in order to stabilize numerical simulations. Two different filtering strategies are employed, one filtering of the pressure field, denoted by $\overline{\left| \cdot \right|}_p$ and another filtering of the density field, denoted by $\overline{\left| \cdot \right|}_\rho$. The pressure filtering $\overline{\left| \cdot \right|}_p$ does not affect the simulation accuracy and has been used every iteration of the numerical simulations. The density filtering $\overline{\left| \cdot \right|}_\rho$ on the other hand can affect the temporal convergence of the solution and its overuse can change the dynamical features of the solution, by creating an artificial diffusion of density. Therefore a strategy to use density filtering $\overline{\left| \cdot \right|}_\rho$ after every specified number of iterations (typically on the order of tens of iterations) is used for the simulations. This in effect allows the local spurious oscillations to grow nominally for certain physical time and then the density filtering $\overline{\left| \cdot \right|}_\rho$ is applied. The time advancement algorithm and solution filtering has been validated using the shock tube test case with an ideal gas detailed in [Sarkar \(2019\)](#).

The implemented homogenous mixture model for cavitating flow is validated by considering the spherical collapse of a 2D bubble (radial collapse of a cylindrical bubble). The analytical Rayleigh equation in 2D in eq. (18) is derived from the

continuity equation in a cylindrical coordinate system (r, θ, z) , where \dot{R} is the time derivative of bubble radius $R(t)$ with respect to time t , p_v is the vapor pressure and $p(R_b, t)$ is the pressure at any position of domain boundary R_b . It is important to note that in eq. (18) R_b cannot be taken as infinite to assume a pressure condition applied at infinity due to the logarithmic singularity in the equation. Therefore, a finite cylindrical domain of radius R_b is taken to compute the evolution of a 2D bubble collapsing under the influence of pressure p at the boundary.

$$(R\ddot{R} + \dot{R}^2)\ln\frac{R_b}{R} - \frac{\dot{R}^2}{R}\left(1 - \frac{R^2}{R_b^2}\right) = \frac{p_v - p(R_b, t)}{\rho} \quad (18)$$

The numerical simulation is done with a circular domain in the $x - y$ coordinate, which is assumed to extend infinitely in z direction with outlet boundary condition on the domain boundary. A $1/4^{th}$ symmetrical domain is also considered, thus reducing the computational domain by virtue of using two symmetrical planes. The bubble is initialized with 100 cells along its radius for both the full and $1/4^{th}$ symmetrical test case. The numerical results for 2D vapor bubble collapse of initial bubble radius $R_0 = 500 \mu m$, $\alpha = 0.99$ at pressure $p_v = 2194 Pa$, surrounded by liquid pressure $p = 10 MPa$, $\alpha = 0$ is compared with the analytical result in fig. 5. The analytical result is derived for a vapor pressure $p_v = 2194 Pa$ and for domain boundary location $R_b = 17R_0$. The non-dimensionalized temporal evolution of bubble radius R plotted is resolved every $0.05 \mu s$ except the last three points which are resolved at every $0.25 \mu s$. The analytical and numerical result in the plot are non-dimensionalized using the initial bubble radius R_0 and collapse time measured from the analytical solution, referred in this case as $t_{rayleigh} = 8.75 \mu s$ for $R_b = 17R_0$. The numerical bubble radius is estimated from the evolving area (since in 2D) of the bubble, with the bubble interface defined at $\alpha = 0.5$ while the vapor volume fraction α is depended on the transported density. The

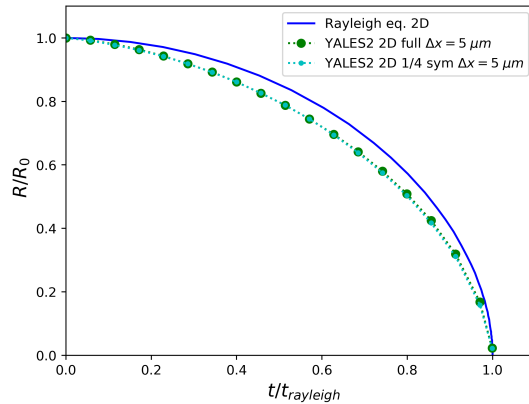


FIGURE 5: 2D Rayleigh collapse comparison for $R_b = 17R_0$ ($t_{rayleigh} = 8.75 \mu s$), initial bubble radius $R_0 = 500 \mu m$.

numerical results give reasonable agreement with the analytical results, specifically

the total duration of the bubble collapse is well captured for the case of $R_b = 17R_0$. There is some deviation in the predicted bubble radius in our numerical simulation compared to analytical result, which is attributed to the difference between the initial conditions assumed in the Rayleigh solution and the ones implemented through the barotropic model.

Indeed, the analytical Rayleigh solution assumes a bubble in equilibrium with surrounding liquid pressure kept very close to vapor pressure p_v while the domain boundaries are at a higher pressure $p(R_b, t)$ with the pressure increasing towards the boundary. On the other hand, the barotropic assumption does not allow to simulate the liquid state at vapor pressure, so the bubble in the numerical set up is surrounded by a nearly uniform liquid pressure of 10 MPa from the bubble interface to the domain boundary. Similarly, 3D vapor bubble collapse is validated against the Rayleigh-Plesset equation (Franc and Michel (2006)) discussed elaborately in Sarkar (2019).

2.2. Solid mechanics solver

The role of solid mechanics computations is to predict the stress and displacements inside a deformable body subjected to the action of forces and/or displacements at its boundary. Here, the solid material response and surface deformation prediction from impacting cavitation loads are carried out with the finite element implicit solver Cast3M. The solver resolve the boundary value problem from the conservation of linear and angular momentum of a deformable continuum. The local equilibrium equations for linear and angular momentum are :

$$\begin{aligned}\nabla \cdot \underline{\underline{\sigma}} + \underline{\underline{f}} &= \rho \underline{\underline{a}}, \\ \underline{\underline{\sigma}} &= \underline{\underline{\sigma}}^T.\end{aligned}\tag{19}$$

Here, $\underline{\underline{\sigma}}$ is the Cauchy stress tensor, $\underline{\underline{f}}$ is the body forces, ρ is the material density, $\underline{\underline{a}}$ is the material acceleration and the superscript T denotes the transpose. In cavitation erosion, on one hand, the pressure loading varies over time and on the other hand, the importance of the forces of inertia has to be considered. Therefore, the dynamic response of the solid has to be predicted. The deterministic implicit solver in Cast3M (Di Paola et al. (2017a)) has been used to solve the non-linear dynamic solid mechanics problem. Considering a static non-linear problem of small deformation on a domain Ω , the equilibrium equation, constitutive law and small deformation assumption gives :

$$\nabla \cdot \underline{\underline{\sigma}} + \underline{\underline{f}} = \underline{\underline{0}},\tag{20}$$

$$\underline{\underline{\sigma}} = \underline{\underline{C}} : \underline{\underline{\varepsilon}}_e = \underline{\underline{C}} : (\underline{\underline{\varepsilon}} - \underline{\underline{\varepsilon}}_p)\tag{21}$$

$$\underline{\underline{\varepsilon}} = \frac{1}{2}(\nabla \underline{\underline{u}}_d + \nabla (\underline{\underline{u}}_d)^T)\tag{22}$$

Eq. (21) is Hooke's law where $\underline{\underline{\sigma}}$ and $\underline{\underline{\varepsilon}}$ are the second order stress and strain tensor, $\underline{\underline{C}}$ is the 4th order stiffness tensor, u_d is the displacement, $\underline{\underline{\varepsilon}}$ is the total strain decomposed in terms of elastic and plastic strain components $\underline{\underline{\varepsilon}}_e$ and $\underline{\underline{\varepsilon}}_p$ respectively. After domain integration of the weak form of the equilibrium equation, the spatial discretization of the finite element method leads to a system of equations given in eq. (23), where \underline{F} is the equivalent nodal force vector and \underline{B} is the discretized gradient operator defined from the element shape functions.

$$\int \underline{B}^T \underline{\underline{\sigma}} dV = \underline{F} \quad (23)$$

For each time step, the equilibrium is found by minimizing the residual $\underline{R} = \underline{F} - \underline{B}^T \underline{\underline{\sigma}}$. This is obtained through an iterative prediction-correction algorithm where the displacement solution of the problem is first initialized via the elastic prediction $\underline{U} = \underline{K}^{-1} \underline{R}$ with \underline{K} the tangent linear stiffness at the beginning of the step. The strain tensor is then evaluated and the internal variables (here the cumulated plastic strain) are updated which gives a new estimation of the stress tensor $\underline{\underline{\sigma}}$ and consequently a new residual \underline{R} .

After introduction of inertial and viscous effect, the finite element system transforms into :

$$\underline{M} \cdot \ddot{\underline{U}} + \underline{D} \cdot \dot{\underline{U}} + \int \underline{B}^T \underline{\underline{\sigma}} = \underline{F} \quad (24)$$

where $\dot{\underline{U}}$ and $\ddot{\underline{U}}$ are the nodal velocity and acceleration vectors, \underline{M} is the mass matrix and \underline{D} is the damping matrix. Equation (24) can be interpreted as the static equilibrium equation with added inertial forces ($-\underline{M} \cdot \ddot{\underline{U}}$) and viscous forces ($-\underline{D} \cdot \dot{\underline{U}}$). This equation is resolved using an implicit time algorithm.

The dynamic formulation will be used for the prediction of deformation of solid from the temporal evolution of stresses on cavitation bubble collapse. In this paper, the FEM simulations are conducted in 2D plane-strain conditions in order to be consistent with the infinite third dimension assumed for the fluid domain.

Three different materials, namely aluminum alloy (Al-7075), duplex stainless steel (St A-2205) and nickel-aluminum-bronze (NAB) are considered to estimate the material response. For the three materials, the elastic regime is assumed as a linear isotropic behavior described by the Young modulus E and Poisson ration ν up to the initial yield stress σ_y . The plastic regime is described by a Von Mises yield criterion with an isotropic hardening function known as *Ludwik equation* :

$$\sigma_{VM} = \sigma_y + K \varepsilon_p^n \quad (25)$$

where the constant K is the strength coefficient, n is the strain hardening exponent and ε_p is the accumulated equivalent plastic strain.

Data for material properties and yield strength summarized in table 2, are taken from Roy et al. (2015) which were obtained with compression tests at a strain rate of 1.0 s^{-1} . The material behavior for Al-7075, St A-2205 and NAB are shown together in fig. 6 for comparison.

Material	ρ [kg/m^3]	E [GPa]	ν	σ_y [MPa]	K [MPa]	n
Al-7075	2810	71.9	0.33	500	312	0.29
St A-2205	7805	186	0.30	560	917	0.51
NAB	7580	122	0.32	300	1205	0.56

TABLE 2: Material density, Young’s modulus, Poisson’s ratio and compressive properties at strain rate $1.0 s^{-1}$ (Roy et al. (2015)).

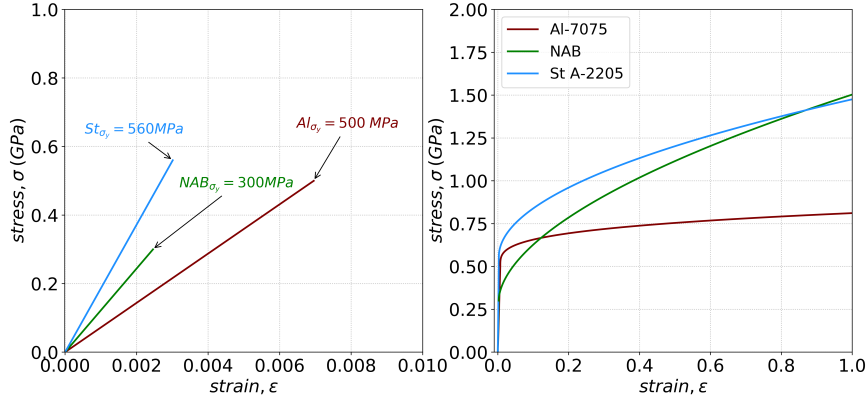


FIGURE 6: Stress-strain curves for Al-7075, St A-2205 and NAB at strain rate $1.0 s^{-1}$.

2.3. Fluid-structure interaction : One-way coupling

In fluid-structure interaction (FSI) problems, solid structures interact with the surrounding fluid flow. The partitioned approach also known as the staggered approach, used in this work, treats the fluid and solid independently with respective numerical algorithms and interfacial conditions are used to exchange information between fluid and solid solutions. Two solvers deal respectively with the fluid and solid mechanics equations and exchange information at the interfaces. The partitioned approach allows for different time steps for the fluid and solid that could be optimized to resolve the different time scales of the two domains. The challenge is, however, to coordinate the algorithms to achieve accurate and efficient fluid-structure interaction solution by keeping the two codes uncoupled.

The approach pursued in this paper is the uncoupled analysis called the one-way fluid-structure interaction. The fluid domain is modelled alone by assuming a rigid boundary in place of the solid. To this end, a purely CFD solver is used which computes the pressure distribution $p(x, t)$ as a function of space x and time t along the fluid solid interface for the entire time duration of interest. Next, the computed pressure $p(x, t)$ is used in a separate calculation as time-dependent boundary condition to load a deformable solid resolved with the CSM solver. This in return gives the time-dependent response of the solid to the applied loads, as represented in fig. 7.

The bubble collapse dynamics is solved with the semi-implicit CFD algorithm

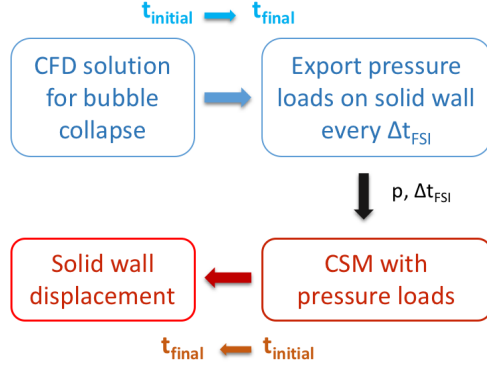


FIGURE 7: One-way FSI procedure.

from initial time t_{in} to final time t_{fin} with the pressure loads on the solid wall extracted at equally spaced time intervals Δt_{FSI} . Let this be referred as *CFD step 1*. The pressure loads are then used as a time-dependent boundary condition to advance the CSM computation from t_{in} to t_{fin} in *CSM step 1*. Only one step of CFD and CSM computations are performed and this provides the solid state at the end of the entire simulation as well as during the transients of the bubble collapse.

3. Bubble collapse dynamics

The dynamics of 2D circular bubbles collapsing at different distances from a planar solid wall are investigated for shock-induced collapse. A shock-induced collapse refers to vapor bubble collapse induced by a shock wave propagating over the bubble. A computational domain of size $10R_0 \times 5R_0$ is considered, where R_0 is the initial bubble radius and taken as $R_0 = 500 \mu m$. We take advantage of symmetries by simulating only one-half of the 2D bubble in all the cases considered. The bubble is resolved within in a region of uniformly spaced quadrilateral cells with $\Delta x = \Delta y = 5 \mu m$ whereas the exterior domain has unstructured quadrilateral cells. Grid stretching is applied with a growth ratio of 1.05 towards the outlet boundary with around 500,000 computational cells in the entire fluid domain. The solid wall is located at the bottom of the computational domain. The outlet boundaries are located at $10R_0$ in the positive x-direction and at $5R_0$ in the y-direction. The outlet boundaries are equipped with Navier-Stokes Characteristic Boundary Conditions (NSCBC) following [Poinsot and Lele \(1992\)](#). The NSCBC boundary conditions allow the domain boundaries to be weakly reflective in our viscous multi-dimensional simulation. Importantly the propagation of waves on the NSCBC-equipped boundaries is treated only in the boundary normal direction. A spherical wave originating in the domain center, near the dynamical bubble collapse region, will become nearly planar due to increased wave front ra-

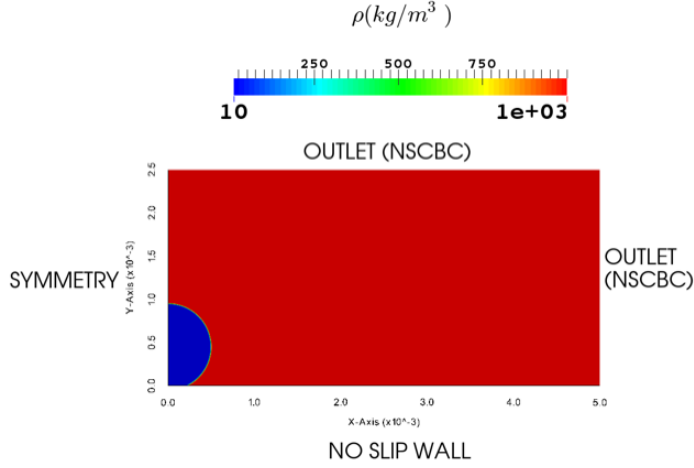


FIGURE 8: Computational domain for 2D bubble collapse - domain boundary $10R_0 \times 5R_0$, domain size = $5 \times 2.5 \text{ mm}^2$.

dius as it approaches the boundaries located far, so that the previous assumption is acceptable. Care needs to be taken anyway concerning the junction between two differently oriented boundaries at the corners of the domain. Here, spurious numerical artefacts may arise and propagate along the bisector. Therefore, the domain length in the x-direction has been chosen to be twice as long as the one in the y-direction.

In the single-fluid cavitation model, a bubble is initialized with a hyperbolic tangent profile which assumes a continuous evolution of density through the interface given in eq. (26). Here Δx is the computational mesh spacing and d_f is the analytical distance function to the interface in eq. (27), x_i is the spatial coordinate, x_c is the position of the bubble center, ρ_v is the liquid-vapor mixture density corresponding to p_v^{sat} and ρ_l is the liquid density. The pressure at initialization is obtained depending on ρ_v and ρ_l from eq. (13) & (14).

$$\rho_{init} = \rho_v + \left(\frac{\rho_l}{2} + \frac{\rho_l}{2} \times \tanh \left(\frac{d_f}{\Delta x} \right) \right) \quad (26)$$

$$d_f = \sqrt{\sum_{i=1}^{N_{dim}} (x_i - x_c)^2} - R_0 \quad (27)$$

The bubble is initially resolved with 100 computational cells in the initial bubble radius. The simulations are carried out with the semi-implicit CFD solver with a limiting $CFL = 0.01$ and $CFL_{acou} = 0.5$ giving a time-step Δt smaller than 1 ns for the entire simulation. The small value of limiting CFL is to ensure numerical stability of the time advancement scheme in our cavitation modelling where the fluid density decreases steeply at the phase interface. The smallest Δt of about

0.05 *ns* is during the most dynamical part of bubble collapse, when the liquid jet velocity is very high ($> 500 \text{ m/s}$) and multiple shock waves propagate in the domain. The total simulation time for bubble collapse and subsequent material response is $t_{fin} = 6 \mu\text{s}$. A 4th order artificial viscosity model with a artificial viscosity constant of 0.1 is used, along with density filtering ($\overline{(\cdot)}_\rho$) every 40 time iterations and pressure smoothing by ($\overline{(\cdot)}_p$) at every iteration. It is important to mention again that the smoothing and filtering steps are needed for solution stability and have been extensively tested to have negligible impact on the solution accuracy.

We will quantify the effects of bubble collapse on resulting wall pressure at different non dimensional stand-off distance $\gamma = h/R_0$, where h is the distance between the solid wall and bubble center. Based on γ , the bubble position with respect to the wall can be categorised as attached ($\gamma \leq 1$) and detached ($\gamma > 1$) bubbles. An attached bubble is initially defined as a circle cut by a plane due to the presence of the wall. For such cases, R_0 is the radius of a perfectly spherical bubble that would have the same volume (surface in 2D) as the non-spherical attached bubble.

We will present 2D collapse dynamics for attached ($\gamma = 0.9$, $R_0 = 495 \mu\text{m}$) and detached ($\gamma = 1.4$, $R_0 = 500 \mu\text{m}$) vapor bubbles surrounded by water at atmospheric pressure. A shock front is initiated at a distance of 2 *mm* from the solid wall and initially both fluids are at rest :

$$\begin{aligned} \text{vapor} : \rho &= 10 \text{ kg/m}^3, p = 2194 \text{ Pa}, \\ \text{liquid} : \rho &= 998.2 \text{ kg/m}^3, p = 101,325 \text{ Pa}. \end{aligned} \tag{28}$$

3.1. Attached bubble ($\gamma = 0.9$)

The vapor bubble is attached to the solid wall and the distance between the bubble center and shock front is 1.55 *mm*. On initialization, a shock front with an amplitude of 50 MPa hits the bubble upper surface at $t = 0.68 \mu\text{s}$. The shock front finally hits the solid wall at $t = 1.3 \mu\text{s}$ and is reflected back in the domain. The temporal evolution of a shock-induced attached bubble dynamics is shown in fig. 9. The left half of each frame shows the density contour whereas the right half shows the pressure contour. At 4.2 μs , the bubble surface area has shrunk to approximately 5% of the initial surface and a liquid jet is formed from the bubble upper boundary. The bubble shapes shown in the density contour matches with the experimental observations of bubble collapse presented in fig. 10.

To quantify the wall pressure and relate it to the bubble dynamics, we will look into the temporal evolution of pressure in fig. 11. The plot shows two curves, one is the evolution of pressure p_{F00} on the wall at the axis of symmetry, denoted by the point $F00$ in fig. 12. The second curve corresponds to the temporal evolution of instantaneous maximum pressure on the solid wall, denoted by $p_{max-wall}$. It should be noted that $F00$ is a point fixed in space, but this is not the case for the

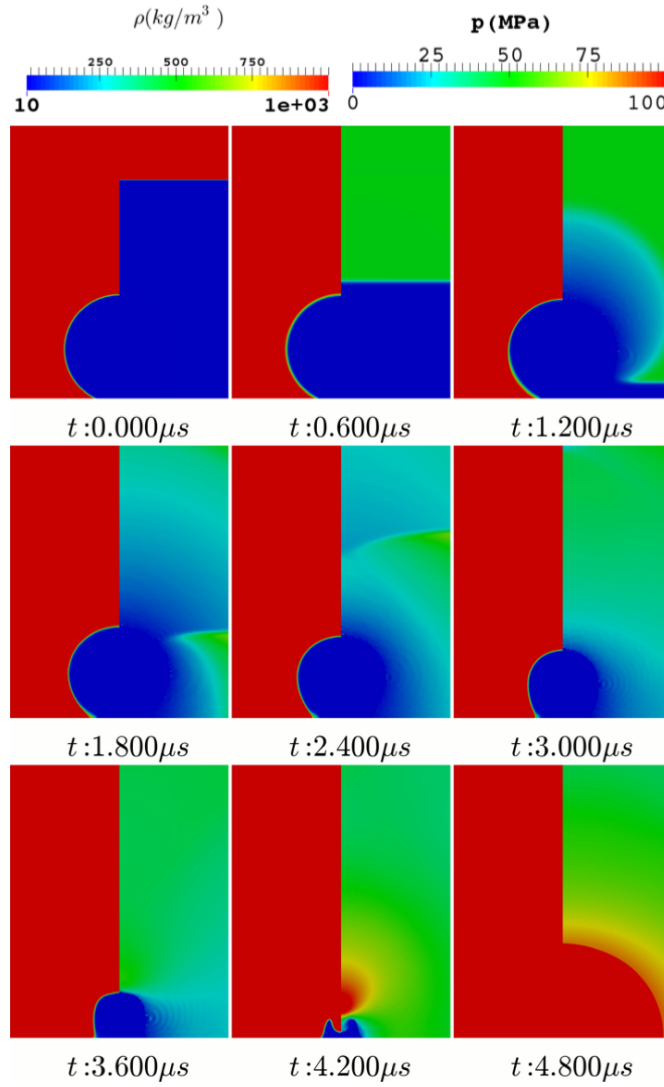


FIGURE 9: 2D attached bubble : (*left*) density and (*right*) pressure contour on each frame showing temporal evolution of a shock-induced 2D bubble collapse, $\gamma = 0.9$, $R_0 = 495 \mu m$, $p = 0.1 MPa$, $p_{shock} = 50 MPa$, frame size = $2 \times 2.5 mm^2$.

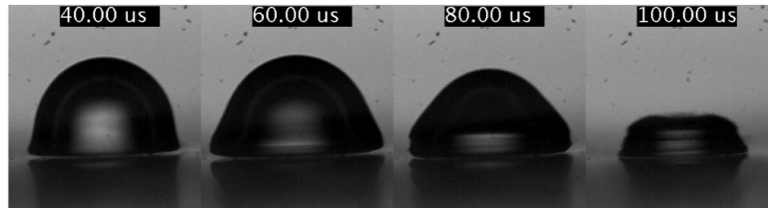


FIGURE 10: Experimental images for attached bubble collapse in atmospheric condition $\gamma = 0.55$, $R_{max} = 400 \mu m$ (Sarkar (2019)).

location of the points contributing to $p_{max-wall}$. The other point in fig. 12 is $F10$ located on the solid wall at a distance of 1 mm from the axis of symmetry. This 1 mm wall length between point $F00$ and $F10$ on the fluid boundary is resolved with 201 equally spaced computational nodes. There are three major pressure peaks, each representing an important characteristic of the bubble collapse.

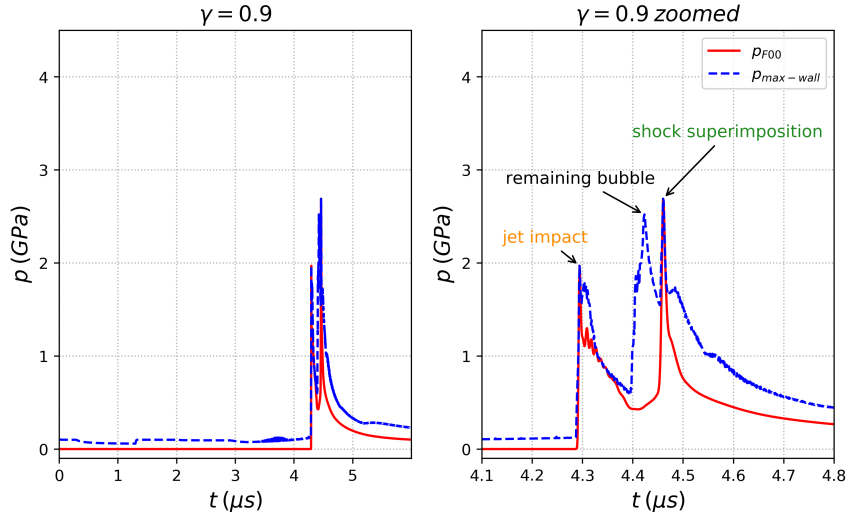


FIGURE 11: 2D attached bubble : pressure peaks at p_{F00} and $p_{max-wall}$ on the solid wall for shock-induced collapse, $\gamma = 0.9$.

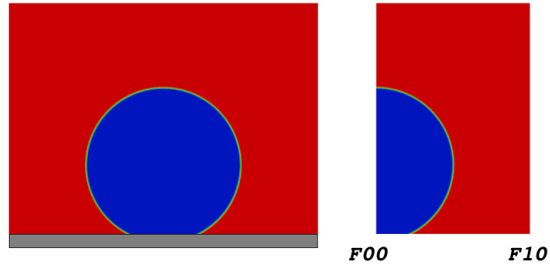


FIGURE 12: Location of probe points on the solid wall : $F00(x, y) = (0, 0)$ and $F10(x, y) = (0.001, 0)$.

The first peak of 1.97 GPa at $4.294\ \mu\text{s}$ is the so-called water hammer pressure p_{wh} due to the liquid jet impact on the solid wall. This pressure can be expressed as $p_{wh} = \rho c u_{jet}$, where ρ is the liquid density, c is the speed of sound and u_{jet} is the liquid jet velocity at impact. The local flow condition at the moment of collapse in the impact location is density $\rho = 1300\text{ kg/m}^3$, speed of sound $c = 3000\text{ m/s}$ and jet velocity 500 m/s , giving a theoretical water hammer pressure of 1.95 GPa exhibiting a very good agreement with our numerical result. This illustrates how very high pressure and velocities are achieved in the liquid during collapse. The

liquid jet impact produces a shock wave, referred to as water hammer shock, originating at the point where the liquid jet hits the wall. This simultaneous effect of the jet flowing outwards after the impact with the wall and the shock wave starts to collapse the remaining bubble (2D equivalent of a 3D torus) still attached to the wall seen in fig.13. The remaining bubble is also deformed by the

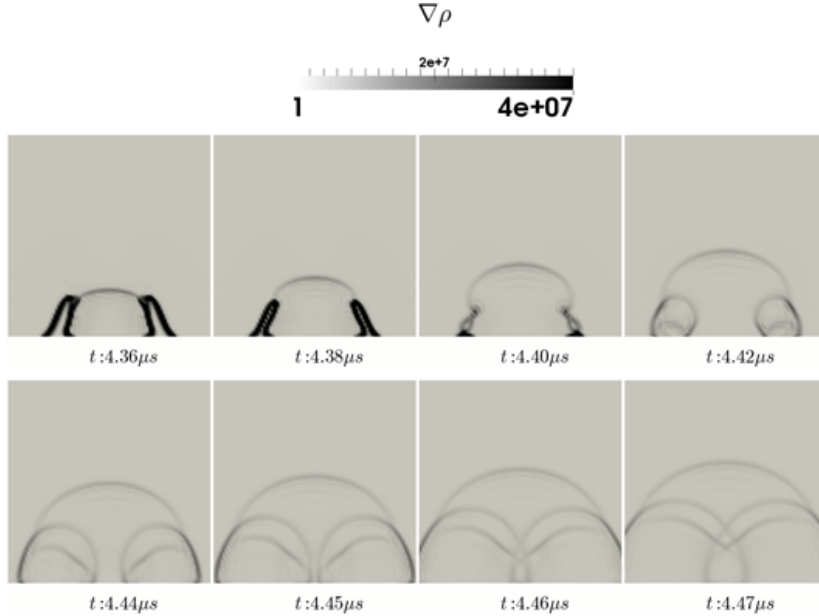


FIGURE 13: Numerical schlieren showing the sequence of events during the remaining bubble collapse-emission of primary and secondary shock, shock induced attached bubble collapse $\gamma = 0.9$, $R_0 = 495 \mu m$, $p = 0.1 MPa$, $p_{shock} = 50 MPa$, frame size = $500 \times 500 \mu m^2$.

inward movement of the surrounding flow induced by the collapsing bubble.

The second pressure peak of 2.52 GPa on the solid wall at $t = 4.423 \mu s$ is due to the remaining bubble collapse at an offset of 0.1 mm from the bubble symmetry axis. The pressure evolution at different time instants on the solid wall is shown in fig. 14.

The shock waves emitted from the remaining bubble collapse travel along the wall towards the bubble symmetry axis, giving the third pressure peak of 2.69 GPa at $t = 4.46 \mu s$ from the superimposition of shock waves and strong compression of liquid in the center region. Finally, this shock wave from the bubble center travels radially along the wall and in the computational domain attenuating in magnitude with increasing distance from bubble center.

Few important observations can be made regarding the remaining bubble collapse taking place at an offset of 100 μm from the bubble symmetry axis. The remaining bubble collapse is driven by two mechanisms : firstly the inward-moving flow, induced by the collapsing bubble which pushes the bubble surface towards the symmetry axis. The second mechanism is the liquid jet flow propagating out-

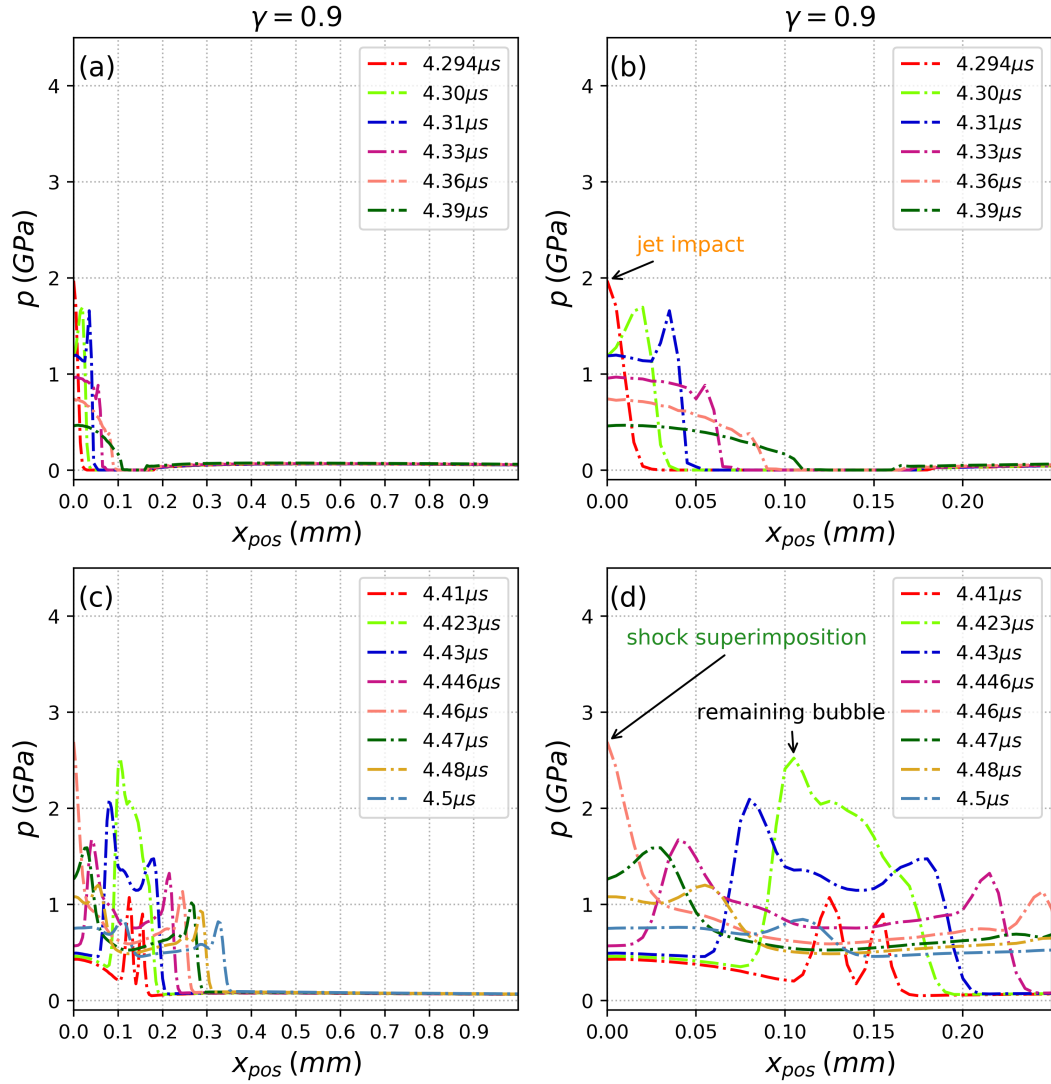


FIGURE 14: 2D attached bubble : pressure plots on the solid wall between points $F00$ and $F10$ at different time instants, shock induced attached bubble collapse $\gamma = 0.9$, $R_0 = 495 \mu m$.

wards from the symmetry axis along the wall, which pushes the remaining bubble away from the symmetry axis. This can be seen in the velocity field shown in fig. 15. Once the remaining bubble collapses, a recirculation zone in the flow field is generated close to the symmetry axis and the wall. Such a recirculation is sustained during the rest of the dynamical part when the shock wave compresses the liquid on the symmetry axis and travels towards the side and top boundaries.

Secondly during the remaining bubble collapse, the importance of boundary layer development can be seen in fig. 13. The remaining bubble collapse is split into two parts by outward travelling liquid flow on the solid wall after the jet impact. Due to the development of boundary layer, the fluid flow very close to the solid wall moves at a slower velocity as compared to the rest of the outward flowing liquid jet along the wall. A maximum flow velocity $u_x = 900 \text{ m/s}$ in the mesh cell and local cell Reynolds number $Re_x = 4500$ is computed for the outward flowing liquid jet. The fast-moving liquid flow on the wall surface splits the remaining bubble into two parts (fig. 13). A top part collapses first, at $t = 4.40 \mu\text{s}$, with the emission of a primary shock wave. The rest of the remaining bubble attached to the solid collapses next, at $t = 4.42 \mu\text{s}$, producing a secondary shock wave. Both the primary and secondary shock waves travel radially outwards from the location of remaining bubble collapse. It is worth mentioning that in our investigation, the first grid point in the solid wall normal direction is located at a distance of $\Delta y = 5 \mu\text{m}$. Therefore, the wall shear stress from the liquid jet flow has not been reported as it would require much finer mesh in the wall normal direction to resolve the boundary layers accurately. According to Zeng et al. (2018), the wall shear stress is of the order of 100 kPa from the liquid jet flow along the solid wall for a bubble $R_0 = 50 \mu\text{m}$ at $\gamma = 1$, resolved with a much finer mesh of first grid point at $\Delta y = 0.1 \mu\text{m}$.

3.2. Detached bubble ($\gamma = 1.4$)

In the case of detached cavity for $\gamma = 1.4$, the shock hits the bubble upper surface at $t = 0.51 \mu\text{s}$, as it can be seen in figure 16. The bubble upper surface flattens and moves towards the shock propagation direction i.e. towards the solid wall. The shock front inducing the bubble collapse is reflected back from the solid wall and interacts once more with the collapsing bubble. This interaction happens at a relatively early stage of collapse, therefore this reflected shock does not retard the formation of liquid jet in our simulation. During the final stages, the liquid jet is formed compressing the bubble upper surface along the symmetry axis. The evolving shape of the bubble matches well with the experimental observations as can be seen in comparing fig. 16 & 17 for $\gamma = 1.4$.

In the final stages, the liquid jet is pushing the bubble upper surface which collapses with the bubble lower surface resulting in the emission of a shock wave. The shock produced is a water hammer shock from the liquid jet travelling with the bubble upper surface collapsing on the bubble lower surface and the shock

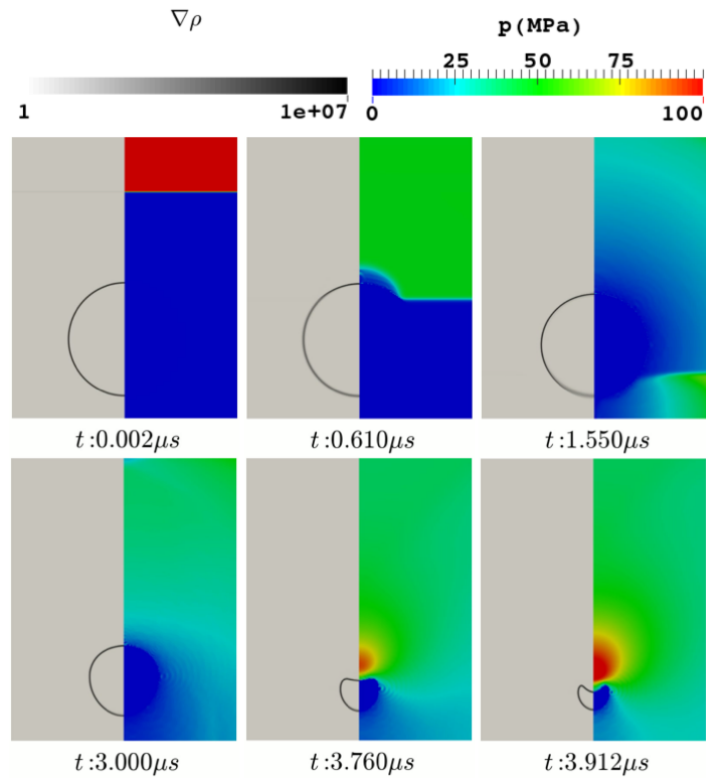


FIGURE 16: 2D detached bubble : bubble shapes in numerical simulation $\gamma = 1.4$, $R_0 = 500 \mu m$, $p = 0.1 MPa$, $p_{shock} = 50 MPa$.

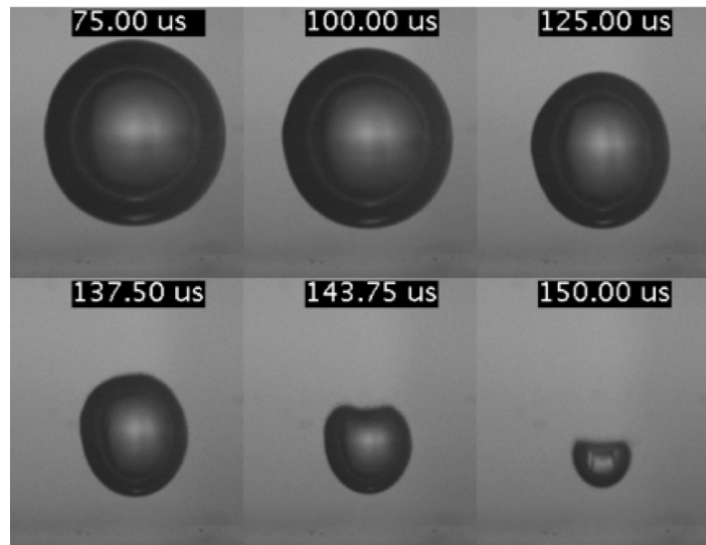


FIGURE 17: Detached bubble collapse : bubble shapes in experimental images, $\gamma = 1.4$, $R_0 = 730 \mu m$ (Sarkar (2019)).

subsequently propagates towards the solid wall. The maximum liquid jet velocity is 750 m/s at $t = 4.1 \mu\text{s}$ which decelerates upon the collapse of the bubble upper surface on the lower surface. Such generation of water hammer shock has been reported experimentally by Lindau and Lauterborn (2003) and numerically by Johnsen and Colonius (2009). At $t = 4.20 \mu\text{s}$ in fig. 18, the shock speed of the water hammer shock is 2400 m/s which is propagating in a liquid almost at rest towards the solid wall. Along with the water hammer shock travelling towards the

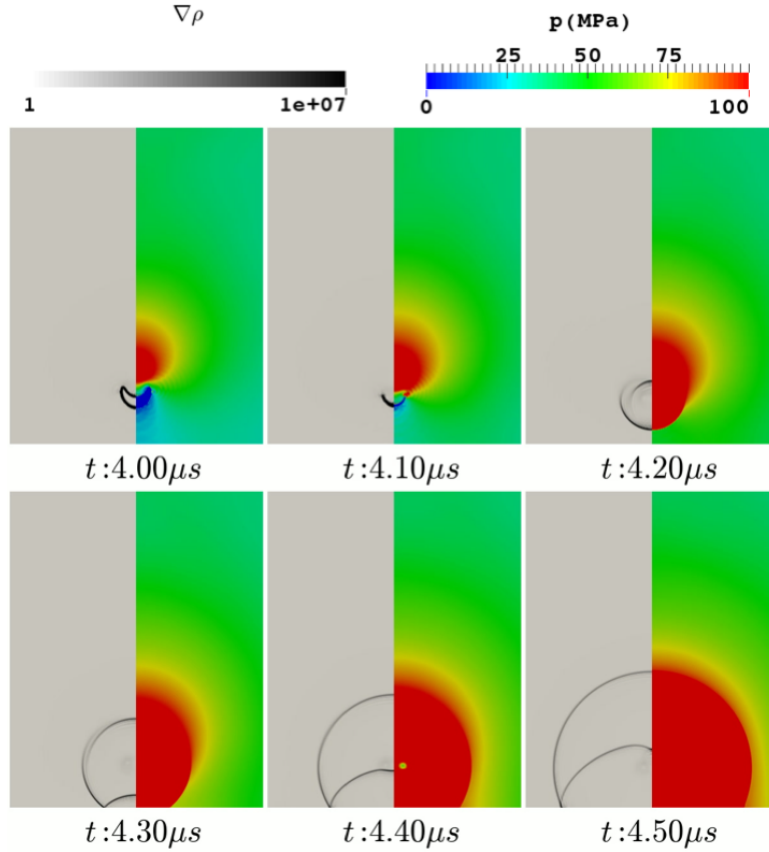


FIGURE 18: 2D detached bubble : final stages of collapse showing shock propagation near the solid wall $\gamma = 1.4$, $R_0 = 500 \mu\text{m}$, $p = 0.1 \text{ MPa}$, $p_{shock} = 50 \text{ MPa}$, frame size = $1 \times 2.5 \text{ mm}^2$.

wall, another shock wave is also created which travels in the opposite direction seen at $t = 4.20 \mu\text{s}$ in fig. 18. The shock wave propagating in the wall-opposite direction is propagating at 2600 m/s in a flow field induced by the collapsing bubble. The water hammer shock impacts the wall with peak pressure of 1.34 GPa at $t = 4.26 \mu\text{s}$ shown in fig. 19 and the impacting shock is reflected back from the solid wall. The reflected shock expands radially with the shock front travelling along the wall and the shock intensity decreases with increasing wall distance from the symmetry axis.

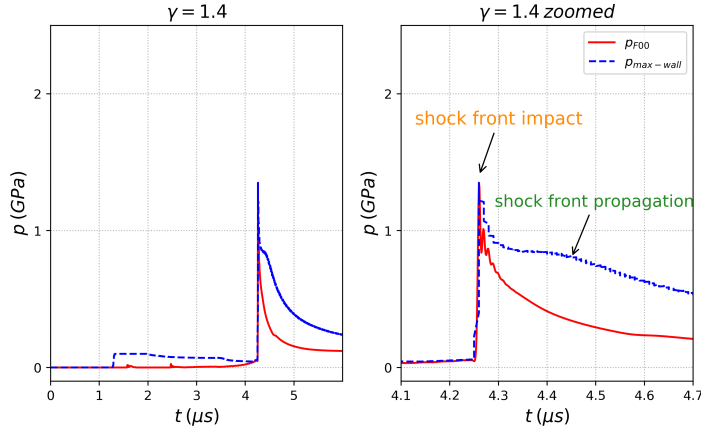


FIGURE 19: 2D detached bubble : pressure peaks at p_{F00} and $p_{max-wall}$ on the solid wall for shock-induced collapse $\gamma = 1.4$, $R_0 = 500 \mu m$.

In our numerical study, we assume that the cavitation bubbles are filled with liquid-vapor mixture only, and that there is no non-condensable gas present inside the bubble. In practical cases, bubbles can entrap the dissolved gases from the liquid water. In such bubble collapses, the bubble volume shrinks due to the higher ambient liquid pressure. Water vapor condensates similarly to what has been discussed until now, but the entrapped non-condensable gas inside the bubble undergoes compression. This first bubble shrinkage is commonly referred to as the first collapse. Due to the high pressures reached inside the bubble during the first collapse in presence of non-condensable gases, the bubble volume grows back again from its state of minimum volume. This phenomenon is commonly referred to as rebound. The collapsing bubble can thus undergo several collapses and rebounds depending on the volume of bubble and non-condensable gas content. In the case of a detached bubble collapse undergoing multiple collapses and rebounds, some part of the gas can move with the induced flow to form smaller satellites bubbles, that can collapse subsequently, possibly very close to the solid wall. Our model does not include the presence of non-condensable gases, and therefore, no rebound is observed. So, in our study we restrict our analysis to the first collapse to understand the liquid-vapor interaction in cavitation.

4. Solid material response

In order to better understand cavitation erosion mechanisms, the response of the solid is now characterized both for attached and detached bubble collapse. We will look into the response of the solid in a one-way coupled approach where the pressure loads generated by the fluid are applied as time-dependent boundary conditions on the solid, with no feedback to the fluid. This has the practical advantage of allowing to perform, firstly a fluid only simulation and subsequently

a solid only simulation. From the point of view of the fluid, this corresponds to assuming the wall to be rigid with infinite impedance, reflecting any incoming wave from the surface.

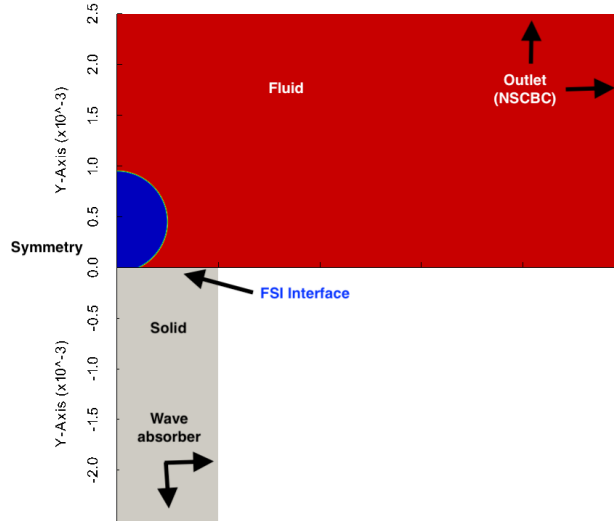


FIGURE 20: FSI coupling domain and interface between the fluid and solid, bubble radius $R_0 = 500 \mu m$, (bottom) solid domain, size = $1 \times 2.5 mm^2$, (top) fluid domain, size = $5 \times 2.5 mm^2$.

We take into consideration the fluid and solid domains as shown in fig. 20. The FSI coupling interface extends only $1 mm$ from the bubble symmetry axis, as most of the dynamical events take place in this region. The use of a much smaller solid computational domain is possible due to the use of wave absorbers on the bottom and right boundaries. The use of larger computational domains for the solid (extending twice as much both in x and y directions) showed no influence on the results. The FEM mesh used for the prediction of the material response is shown in fig. 21. It consists mostly of quadrilateral 8-node elements refined close to the fluid-solid interface. Some horizontal layers of 6-nodes triangular elements ensure the transitions in the mesh sizes. The solid interface of $1 mm$ length is resolved with 801 nodes applying a uniform grid spacing. More nodes are used on the solid interface to resolve accurately the plasticity developed from propagating shock waves with varying shock speed. On the other hand, fluid pressures are obtained on uniformly spaced 201 computational nodes along the considered length of solid wall. Therefore, the fluid pressures are interpolated between the fluid-solid interface with non-matching mesh resolution. The fluid pressures on 201 nodes are interpolated using a quadratic function to the 801 nodes on the solid boundary at the fluid-solid interface.

The plots and contours of our 2D investigation for this symmetrical solid domain is presented for the three materials considered, namely Al-7075, NAB and

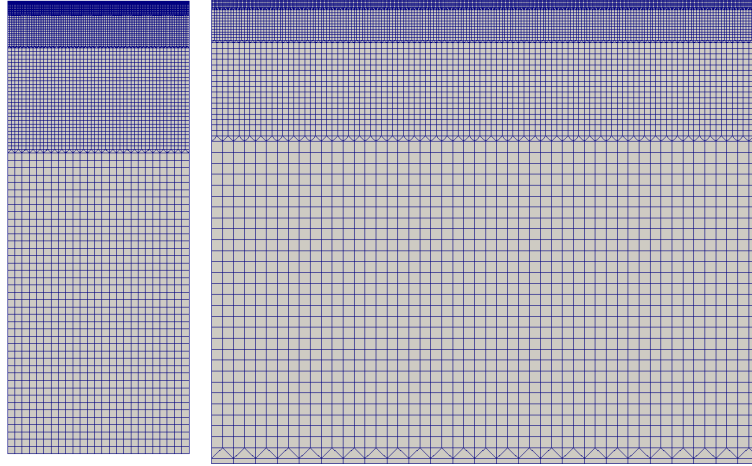


FIGURE 21: Computational domain and mesh used for the FEM simulation - (*left*) full domain, size = $1 \times 2.5 \text{ mm}^2$, $N_{elements} = 9850$, $N_{nodes} = 29065$, (*right*) zoomed view showing transition of fine quadrilateral elements to coarse using layers of triangular elements.

St A-2205. The FSI coupling time is $\Delta t_{FSI} = 5 \text{ ns}$ for the one-way coupling, which means that the fluid pressure is extracted at the rigid wall every Δt_{FSI} for the entire simulation duration and is applied at every Δt_{FSI} on the solid interface as time-dependent boundary condition. It is worth mentioning that time-step independence studies for Δt_{FSI} were performed for the one-way coupling down to $\Delta t_{FSI} = 1 \text{ ns}$ and no difference in the results was observed. At time equal to zero, i.e. prior to applying the pressure load, the solid is considered at rest.

4.1. Attached bubble collapse ($\gamma = 0.9$)

In the case of an attached two-dimensional bubble initially in a liquid at atmospheric pressure, and collapsing under the influence of an impacting 50 MPa shock wave, the solid wall interface position is shown in fig. 22. To recall, only one-half of the problem is simulated taking advantage of the symmetry along the y-axis, and the other solid computational boundaries are treated with wave absorbing characteristics. Wave absorbing boundaries allow the propagation of elastic waves through the boundary in transient dynamic computations (Di Paola et al. (2017b)) and the displacement of FEM nodes at the boundaries equipped with wave absorption is not constrained in the 2D plane i.e. X and Y direction. It physically means that we numerically simulate only a small part of a very large solid material and no reflected elastic waves from the solid boundary reaches our computational domain. This assumption, in return, implies that the solid will be in a continuous state of elastic displacement or compression from the propagation of elastic waves in the solid, since no wave reflection can occur to bring back the solid to a rest state. In other words, there is no relaxation to a rest state in the solid material.

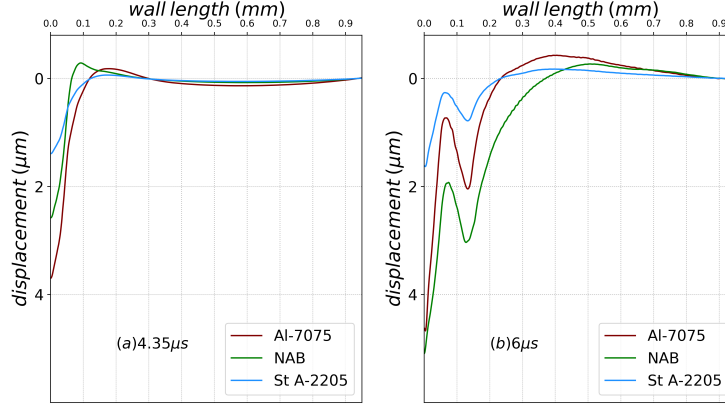


FIGURE 22: Solid wall interface profile. (a) after liquid jet impact $t = 4.35 \mu s$. (b) after entire simulation time $t = 6 \mu s$, $\gamma = 0.9$, $R_0 = 495 \mu s$. The displacement plotted is the difference between the surface displacement and the displacement induced by plane elastic wave.

Therefore, it is important to note that the displacement we present in this paper is the relative displacement defined as the final solid surface displacement minus the displacement induced by the plane elastic wave propagation in the solid domain. The surface node on the solid wall located at 0.95 mm away from the axis does not see any of the dynamic loading from the collapsing bubble and only displaces due to the plane elastic wave. This surface node displacement is taken as the displacement induced by the plane elastic wave and subtracted from solid surface displacement to obtain the relative displacement plotted in fig. 22. The surface node at 1 mm away from axis is not considered due to minor yet observable boundary effects on displacement owing to its position at the intersection between solid wall and wave absorbing boundary.

The liquid jet produces considerable relative displacement at the bubble symmetry axis. The maximum displacement ($3.8 \mu m$) is obtained for Al-7075 specimen, whereas the smallest surface displacement ($1.4 \mu m$) is found for St A-2205 seen in fig. 22 (a). The displacement in NAB from liquid jet impact is $2.6 \mu m$ at the symmetry axis. The temporal convergence of the permanent plastic deformation has been validated to check the convergence in time of the CSM calculations. At the end of the simulation at $6 \mu s$, the maximum plastic deformation has been identified for NAB of $5.1 \mu m$ at the bubble symmetry axis. It is worth mentioning here that the initial yield strength of NAB is 300 MPa , which is the lowest of the three materials considered. For each material, the plastic deformation at the bubble symmetry axis is the cumulative effect of the pressure loads from liquid jet impact and shock wave superimposition. In comparison, we obtain plastic deformation of $4.6 \mu m$ and $1.6 \mu m$ in Al-7075 and St A-2205 respectively. On the other hand, the deformation at an offset of 0.135 mm from symmetry axis is due

to the pressure load from collapse of remaining bubble fragments. The maximum plastic deformation takes place in NAB of $3 \mu m$, followed by Al-7075 of $2.1 \mu m$ and the least deformation in St A-2205 of $0.8 \mu m$ from the remaining bubble fragment collapse. The plastic response of Al-7075 and NAB are similar, whereas St A-2205 clearly offers the maximum resistance to the induced pressure load due to material strength.

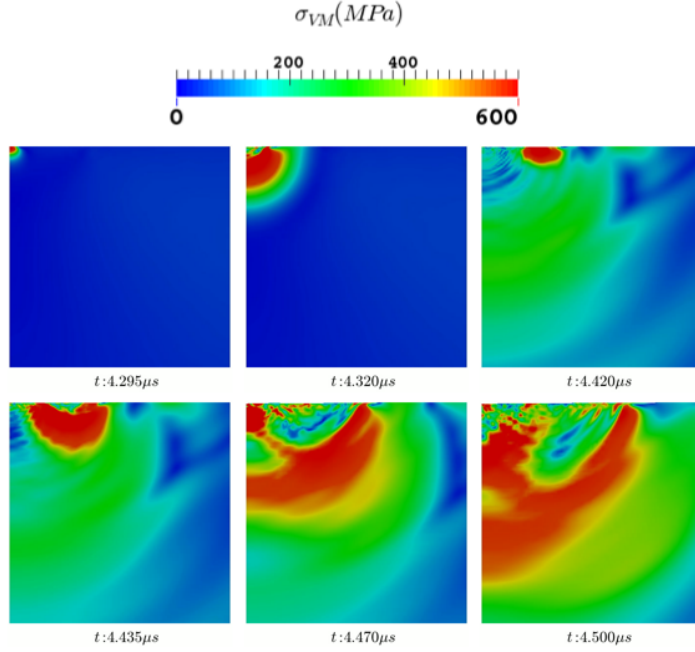


FIGURE 23: von Mises stress σ_{VM} at different time instants during liquid jet impact ($t = 4.295 \mu s$), remaining bubble collapse (2D equivalent of 3D bubble torus at $t = 4.420 \mu s$) and subsequent shock wave superimposition at bubble symmetry axis ($t = 4.470 \mu s$) for St A-2205 ($\sigma_y = 560 \text{ MPa}$), $\gamma = 0.9$, $R_0 = 495 \mu m$, frame size = $1 \times 1 \text{ mm}^2$.

The evolution of von Mises stress (σ_{VM}) in St A-2205 at different stages of the collapse is presented in the snapshots of fig. 23 plotted at $t = 4.295 \mu s$, $4.420 \mu s$ & $4.470 \mu s$ for liquid jet impact, remaining bubble collapse at an offset and shock wave superimposition at the symmetry axis respectively. A value of σ_{VM} greater than the initial yield strength σ_y (560 MPa for St A-2205) indicates the region where the material will yield. To quantify the plasticity developed in the solid, we will draw comparisons on maximum accumulated plastic strain $P_{\varepsilon_p}^{max}$ and surface area under plastic deformation A_{ε_p} . The surface area under plastic deformation A_{ε_p} is computed from the solid surface undergoing plastic strain of at least 0.5% and above. The maximum accumulated plastic strain $P_{\varepsilon_p}^{max}$ for Al-7075, NAB and St A-2205 are respectively 0.255, 0.0972 & 0.0856 whereas the surface area under plastic deformation A_{ε_p} are respectively $5.523 \times 10^{-8} \text{ m}^2$, $9.816 \times 10^{-8} \text{ m}^2$ and $2.052 \times 10^{-8} \text{ m}^2$, as summarized in table 3.

Material	$P_{\varepsilon_p}^{max}$	$A_{\varepsilon_p} (m^2)$
Al-7075	0.255	5.523×10^{-8}
NAB	0.0972	9.816×10^{-8}
St A-2205	0.0856	2.052×10^{-8}

TABLE 3: Maximum accumulated plastic strain $P_{\varepsilon_p}^{max}$ and area under plastic deformation A_{ε_p} for shock induced attached bubble, $\gamma = 0.9$, $R_0 = 495 \mu m$, at $t = 6 \mu s$.

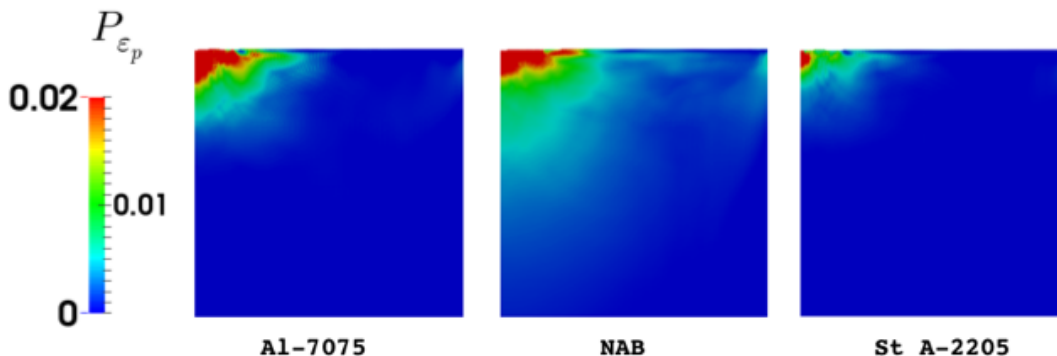


FIGURE 24: Accumulated plastic strain P_{ε_p} for the three considered material at the end of simulation time $t = 6 \mu s$, $R_0 = 495 \mu m$, frame size= $1 \times 1 mm^2$. The symmetry axis is on the left boundary of each image.

The contour of the accumulated plastic strain P_{ε_p} at the end of the simulation (i.e $t = 6 \mu s$), for all the considered materials is shown in fig. 24. For the three materials, the maximum plastic deformation region is located near the bubble symmetry axis where most of the dynamical events takes place. Although the $P_{\varepsilon_p}^{max}$ in Al-7075 is 2.6 times higher than NAB, the A_{ε_p} is highest in NAB i.e. 1.77 times that of Al-7075. This again is related to the material properties considered, where the yield strength of NAB is $\sigma_y = 300 MPa$ whereas for Al-7075, it is $\sigma_y = 500 MPa$. In addition to the plasticity at the bubble symmetry axis, the propagating shock waves on the solid wall lead to the generation of significant plasticity along the length of the solid wall.

4.2. Detached bubble collapse ($\gamma = 1.4$)

In the case of detached bubble at $\gamma = 1.4$, the only impact pressure is the water-hammer shock impacting and travelling on the solid wall. Since there is no bubble rebound considered, at no point does any part of the vapor bubble reaches the wall. The radially propagating shock wave hits on the symmetry axis and travels along the wall. The response of the considered material after the shock wave has propagated along the wall at $t = 6 \mu s$ is shown in fig. 25, where the relative displacement discussed previously is plotted. The solid wall interface undergoes displacement all along the considered wall length, with the maximum

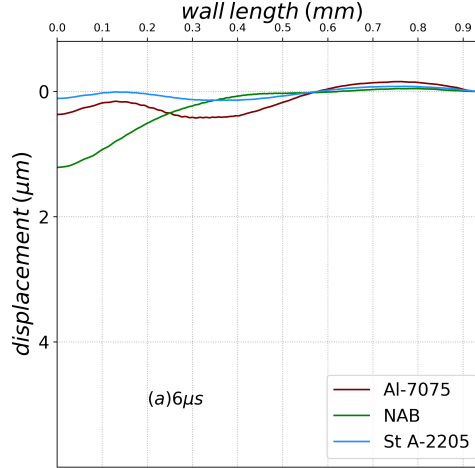


FIGURE 25: Solid wall interface profile after entire simulation time $t = 6\mu s$, $\gamma = 1.4$, $R_0 = 500\mu m$.

plastic deformation of $1.2\ \mu m$ for NAB. At the end of the simulation, only NAB shows a small pit near the symmetry axis whereas the displacement for St A-2205 and Al-7075 demonstrates a wavy solid interface with maximum relative displacement at an offset from the symmetry axis. The region of maximum relative displacement corresponds to the region of maximum accumulated plastic strain $P_{\varepsilon_p}^{max}$ in the solid.

The accumulated plastic strain P_{ε_p} contour for a detached bubble collapse is shown in fig. 26. The region with maximum plasticity is at an offset distance from the bubble symmetry axis for all the three materials. The $P_{\varepsilon_p}^{max}$ in Al-7075 is 0.014 located at a distance of $450\ \mu m$ from the symmetry axis and at a depth of $45\ \mu m$ from the solid surface. Similarly $P_{\varepsilon_p}^{max}$ in NAB and St A-2205 is 0.0109 and 0.00539 respectively, located nearly in the same region in the solid as Al-7075. Using the same definition for area under plastic deformation A_{ε_p} as before, we find plastic surface area of $5.019 \times 10^{-8}\ m^2$, $3.681 \times 10^{-8}\ m^2$ and $6.243 \times 10^{-12}\ m^2$ for Al-7075, NAB and St A-2205 respectively. The values of $P_{\varepsilon_p}^{max}$ and A_{ε_p} are summarized in table 4.

Material	$P_{\varepsilon_p}^{max}$	$A_{\varepsilon_p}\ (m^2)$
Al-7075	0.014	5.019×10^{-8}
NAB	0.0109	3.681×10^{-8}
St A-2205	0.00539	6.243×10^{-12}

TABLE 4: Maximum accumulated plastic strain $P_{\varepsilon_p}^{max}$ and area under plastic deformation A_{ε_p} for shock induced detached bubble, $\gamma = 1.4$, $R_0 = 500\ \mu m$ at $t = 6\ \mu s$.

A few observations can be made : the maximum plastic strain from the im-

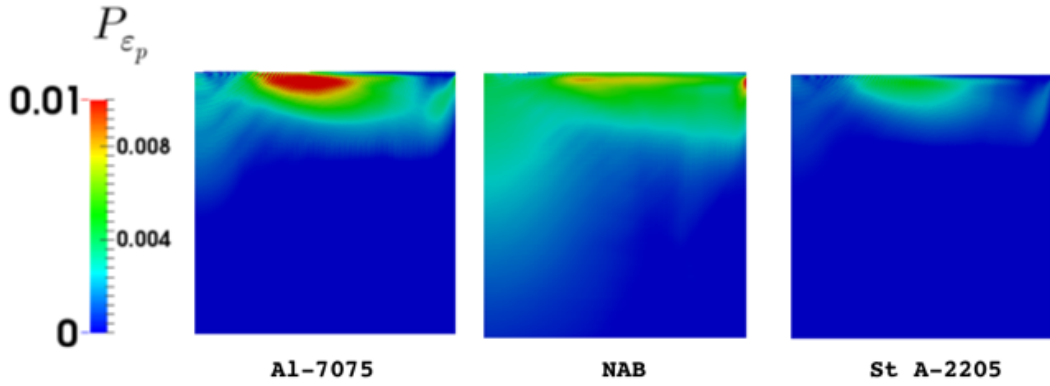


FIGURE 26: Accumulated plastic strain P_{ϵ_p} for the considered material at $t = 6\mu s$, $\gamma = 1.4$, $R_0 = 500\ \mu m$, frame size = $1 \times 1\ mm^2$. The symmetry axis is on the left boundary of each image.

pacting shock wave is found for Al-7075. The maximum plastic strain is located at an offset from the bubble symmetry axis. Such an offset in the maximum plastic strain region has been reported in the doctoral thesis of Paquette (2017) and more recently analyzed in Joshi et al. (2019), where it has been interpreted in terms of solid material characteristic time, as it will be recalled below. Although the maximum plastic strain region is located at an offset, the propagating shock does generate non negligible plasticity all along the length of solid wall. The A_{ϵ_p} is the highest for NAB similar to what is found for attached bubble collapse. A

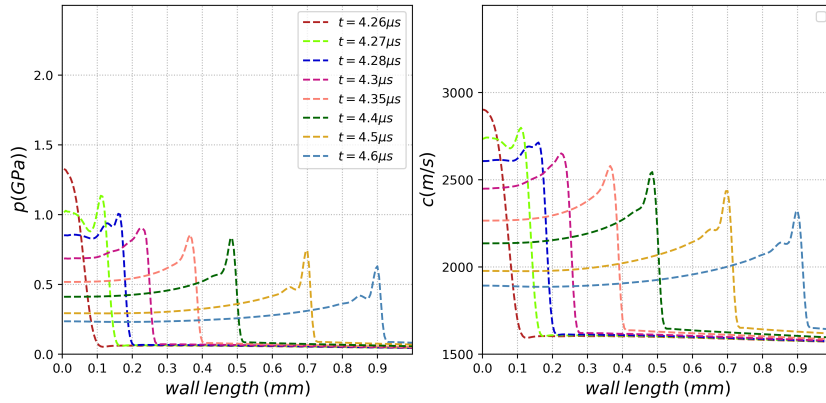


FIGURE 27: Temporal evolution pressure and sound speed on the wall for shock induced detached bubble collapse, $\gamma = 1.4$, $R_0 = 500\ \mu m$.

few points about the propagation of the impact shock wave could be explained here. Comparing it with spatial evolution of pressure, we can essentially see the radially propagating shock wave with its maximum at different location on the wall at different time instants, presented in fig. 27. Looking at the evolution of

the speed of sound c on the wall obtained from fluid calculations, it can be seen that near the symmetry axis, the shock speed on the wall is very high whereas it starts decreasing as the shock moves along the wall after the impact. Then, the offset in the position of the region of maximum plasticity has been attributed to the inertial effects in the solid, where due to high shock speed on the solid surface near the symmetry axis the solid cannot respond fast enough to the pressure load, and the rate of plasticity increases at an offset with decreasing shock speed as the propagating shock wave moves away. The wall shear stress from the high fluid velocity in the wall parallel direction, possibly in the order of few hundred kPa based on literature, could possibly contribute further to the plastic strain at an offset on the solid wall. Despite the fact that the wall shear stress would be many order smaller in magnitude than the propagating shock wave pressure along the wall, one shall recall that plasticity is created by shear in the material, and not by normal stress. As seen previously in the fig. 25, plastic deformation takes place more or less everywhere on the solid interface. The maximum surface displacement is of the order of $1.6 \mu m$ for NAB whereas it is less than $1 \mu m$ for Al-7075 and St A-2205. This is consistent with our observation where NAB absorbs much of the energy from the shock waves and plasticizes more. For a detached bubble collapse, the pit formation is near the symmetry axis for NAB, whereas Al-7075 and St A-2205 undergo pit formation at an offset from the symmetry axis. The overall pit depth in a detached bubble collapse is smaller in comparison to an attached bubble collapse.

5. Conclusions and perspectives

In the course of this work, an investigation on the mechanism of cavitation erosion at the fundamental scale of a single bubble collapse is carried out. The objective is to model the dynamics of collapsing bubbles near rigid and deforming materials and characterize the material response by coupling the fluid and solid mechanics. A compressible cavitation solver is developed in YALES2 for CFD simulation of liquid water and two-phase cavitating flows in 2D and 3D. The compressible *Navier-Stokes* equations are solved together with the equations of state defining all the fluid phases to model small scale as well as large scale cavitating structures efficiently. The solver takes compressibility and viscous effects into account, and uses non-reflective boundary conditions. It is capable of resolving highly dynamic pressure fields generated by violent collapses of vapor structures inside the flow field. The solid mechanics simulations have been performed with the finite-element solver Cast3M to predict the dynamical behaviour of the materials. Wave absorber elements are used to prevent the reflection of elastic waves on the outer boundaries of the simulated domain. The elastic-plastic response of aluminum (Al-7075) alloy, nickel-aluminum-bronze (NAB) alloy and duplex stainless steel (St A-2205), following a power law relationship between stress and strain in the plastic regime, is compared for attached and detached bubble cases.

The dynamics of the bubble collapse has been presented for shock-induced collapse. The dynamic evolution of attached bubbles shows three major events - firstly the liquid jet impact on the solid wall resulting in the water hammer pressure. Secondly the collapse of the remaining bubble (2D equivalent of 3D bubble torus) at an offset from the symmetry axis. Finally the strong compression of liquid at the symmetry axis from the superimposition of the shock waves emitted from the remaining bubble collapse. For a detached bubble, the water hammer shock emitted when the bubble upper surface collapses on the bubble lower surface is the source of pressure loading on the solid wall. Overall, the bubble dynamics has been captured quite accurately for the considered stand-off distances, matching well with the existing literature and experimental data. The magnitude of the pressure loading on the other hand varies depending on the mechanism driving the bubble collapse and the stand-off distance, and has been found to be higher for attached bubble collapse. In the investigation of material response, the attached bubble collapse is found to cause maximum plastic deformation and pit formation at the bubble symmetry axis. The induced plastic deformation results from the liquid jet impact pressure and the interaction of the shock waves arising from remaining bubble collapse. The plastic deformation in detached bubble collapse is located at an offset from the symmetry axis which is attributed to inertial effects in the solid from propagating shock waves. Overall we found higher plastic deformation and pit formation on the solid from a collapsing attached bubble. However, it is obvious that the one-way coupled FSI procedure introduces some approximations as the feedback of solid deformation on the fluid pressure is totally neglected. Therefore, it is possible that under some circumstances, the "true" solid response would be different, nevertheless this provides at least a first-attempt solution of such a complex problem.

The CFD methodology developed for simulation of cavitation has been extensively tested in two dimensions, but its application to three-dimensions is straightforward. An animation of a three-dimensional bubble cloud collapse can be found online³. We generated a random bubble cloud with bubble radii varying from $R_0 = 250 \mu m$ to $R_0 = 500 \mu m$ at different stand-off distances. A larger cloud relevant at the industrial scale would require much larger computational resources and time.

Acknowledgement

This research work was accomplished within the project CaFE⁴ which has received funding from the European Union Horizon 2020 Research and Innovation programme, Grant Agreement No 642536 under the Marie Skłodowska-Curie

3. <https://youtu.be/HpSl7rJOJP4>

4. <http://cafe-project.eu>

Innovative Training Network. We are grateful for this support.

References

- Akcabay, D.T., Young, Y.L., 2014. Influence of cavitation on the hydroelastic stability of hydrofoils. *Journal of Fluids and Structures* 49, 170–185.
- Beattie, D., Whalley, P., 1982. A simple two-phase frictional pressure drop calculation method. *International journal of multiphase flow* 8, 83–87.
- Benjamin, T.B., Ellis, A.T., 1966. The collapse of cavitation bubbles and the pressures thereby produced against solid boundaries. *Philosophical Transactions for the Royal Society of London. Series A, Mathematical and Physical Sciences* , 221–240.
- Blake, J., Gibson, D., 1987. Cavitation bubbles near boundaries. *Annual Review of Fluid Mechanics* 19, 99–123.
- Brennen, C., 1995. *Cavitation and bubble dynamics*. Oxford University Press.
- Brujan, E.A., 2011. *Cavitation in Non-Newtonian Fluids : With Biomedical and Bioengineering Applications*. Springer.
- Choi, J.K., Chahine, G., 2016. Relationship between material pitting and cavitation field impulsive pressures. *Wear* 352, 42–53.
- Cook, A., Cabot, W., 2004. A high-wavenumber viscosity for high-resolution numerical methods. *Journal of Computational Physics* 195, 594–601.
- Di Paola, F., Guerin, C., Berthinier, C., Paredes, R., 2017a. Starting with cast3m thermo-mechanical calculations - training manual.
- Di Paola, F., Guerin, C., Berthinier, C., Paredes, R., 2017b. Pasapas procedure and the users procedures - training manual.
- Egerer, C., Hickel, S., Schmidt, S., Adams, N., 2013. Les of turbulent cavitating shear layers, in : *High Performance Computing in Science and Engineering '13*. Springer, pp. 349–359.
- Franc, J.P., 2009. Incubation time and cavitation erosion rate of work-hardening materials. *Journal of Fluids Engineering* 131, 021303.
- Franc, J.P., Michel, J.M., 2006. *Fundamentals of cavitation*. volume 76. Springer Science & Business Media.
- Franc, J.P., Riondet, M., Karimi, A., Chahine, G., 2012. Material and velocity effects on cavitation erosion pitting. *Wear* 274, 248–259.

- Fujikawa, S., Akamatsu, T., 1980. Effects of the non-equilibrium condensation of vapour on the pressure wave produced by the collapse of a bubble in a liquid. *Journal of Fluid Mechanics* 97, 481–512.
- Gibson, D., 1968. Cavitation adjacent to plane boundaries, in : Proc. 3rd Australasian Conf. on Hydraulics and Fluid Mechanics, Sydney. pp. 210–214.
- Gibson, D., Blake, J., 1980. Growth and collapse of cavitation bubbles near flexible boundaries, in : 7th Australasian Conference on Hydraulics and Fluid Mechanics, Institution of Engineers, Australia. p. 283.
- Gibson, D., Blake, J., 1982. The growth and collapse of bubbles near deformable surfaces. *Applied Scientific Research* 38, 215–224.
- Goncalves, E., Patella, R.F., 2009. Numerical simulation of cavitating flows with homogeneous models. *Computers & Fluids* 38, 1682–1696.
- Hickling, R., Plesset, M., 1964. Collapse and rebound of a spherical bubble in water. *The Physics of Fluids* 7, 7–14.
- Hsiao, C.T., Chahine, G.L., 2015. Dynamic response of a composite propeller blade subjected to shock and bubble pressure loading. *Journal of Fluids and Structures* 54, 760–783.
- Hsiao, C.T., Jayaprakash, A., Kapahi, A., Choi, J.K., Chahine, G., 2014. Modelling of material pitting from cavitation bubble collapse. *Journal of Fluid Mechanics* 755.
- Johnsen, E., Colonius, T., 2009. Numerical simulations of non-spherical bubble collapse. *Journal of fluid mechanics* 629, 231–262.
- Joshi, S., Franc, J.P., Ghigliotti, G., Fivel, M., 2019. Sph modelling of a cavitation bubble collapse near an elasto-visco-plastic material. *Journal of the Mechanics and Physics of Solids* 125, 420–439.
- Kalumuck, K., Duraiswami, R., Chahine, G., 1995. Bubble dynamics fluid-structure interaction simulation by coupling fluid bem and structural fem codes. *Journal of Fluids and Structures* 9, 861–883.
- Kraushaar, M., 2011. Application of the compressible and low-Mach number approaches to Large-Eddy Simulation of turbulent flows in aero-engines. Ph.D. thesis. Institut National Polytechnique de Toulouse-INPT.
- Lauer, E., Hu, X., Hickel, S., Adams, N., 2012. Numerical modelling and investigation of symmetric and asymmetric cavitation bubble dynamics. *Computers and Fluids* .

- Lauterborn, W., Vogel, A., 2013. Shock wave emission by laser generated bubbles, in : Bubble dynamics and shock waves. Springer, pp. 67–103.
- Lindau, O., Lauterborn, W., 2003. Cinematographic observation of the collapse and rebound of a laser-produced cavitation bubble near a wall. *Journal of Fluid Mechanics* 479, 327–348.
- Malandain, M., 2013. Simulation massivement parallèle des écoulements turbulents à faible nombre de Mach. Ph.D. thesis. INSA de Rouen.
- Moureau, V., Bérat, C., Pitsch, H., 2007. An efficient semi-implicit compressible solver for large-eddy simulations. *Journal of Computational Physics* 226, 1256–1270.
- Müller, S., Helluy, P., Ballmann, J., 2010. Numerical simulation of a single bubble by compressible two-phase fluids. *International Journal for Numerical Methods in Fluids* 62, 591–631.
- Naude, C., Ellis, A., 1961. On the mechanism of cavitation damage by nonhemispherical cavities collapsing in contact with a solid boundary. *Journal of Basic Engineering* 83, 648–656.
- Obreschkow, D., Tinguely, M., Dorsaz, N., Kobel, P., De Bosset, A., Farhat, M., 2011. Universal scaling law for jets of collapsing bubbles. *Physical review letters* 107, 204501.
- Paquette, Y., 2017. Interaction Fluide-Structure et Érosion de Cavitation. Ph.D. thesis. Université Grenoble Alpes.
- Poinsot, T., Lele, S., 1992. Boundary conditions for direct simulations of compressible viscous flows. *Journal of computational physics* 101, 104–129.
- Prosperetti, A., 1987. The equation of bubble dynamics in a compressible liquid. *Physics of Fluids* 30, 3626–3628.
- Rayleigh, L., 1917. On the pressure developed in a liquid during the collapse of a spherical cavity. *Philosophical Magazine Series 6* 34, 94–98.
- Reynolds, O., 1894. Experiments showing the boiling of water in an open tube at ordinary temperatures. *Scientific Papers on Mechanical and Physical Subject* 2, 1900–1903.
- Roger, T., Lartigue, G., Moureau, V., 2016. An asymptotic-preserving and semi-implicit pressure-based compressible solver for flows at all mach numbers, in : ERCOFTAC ETMM11 international conference, Sicily, Italy.

- Roy, S., Franc, J.P., Fivel, M., 2015. Cavitation erosion : Using the target material as a pressure sensor. *Journal of Applied Physics* 118, 164905.
- Sarkar, P., 2019. Simulation of cavitation erosion by a coupled CFD-FEM approach. Ph.D. thesis. LEGI, Universite Grenoble Alpes.
- Vantieghem, S., 2011. Numerical simulations of quasi-static magnetohydrodynamics using an unstructured finite-volume solver : development and applications. Ph.D. thesis. Universite Libre de Bruxelles.
- Zeng, Q., Gonzalez-Avila, S., Dijkink, R., Koukouvinis, P., Gavaises, M., Ohl, C.D., 2018. Wall shear stress from jetting cavitation bubbles. *Journal of Fluid Mechanics* 846, 341–355.